Received: 24 September 2025 | Revised: 21 January 2026 | Accepted: 29 January 2026

DOI: 10.1002/VIW.20250211

VIEW

RESEARCH ARTICLE

A thermoplastic microfluidic platform with integrated electrospun scaffolds for assessing brain cell-specific drug selectivity

Maria Testa[1,2] | **Laura Palumbo**[3] | **Martina La Rosa**[1] | **Antonella Girgenti**[3] | **Fabio Salvatore Palumbo**[3,4] | **Pasquale Picone**[3] | **Francesco Lopresti**[1] | **Domenico Nuzzo**[3] | **Vincenzo La Carruba**[1]

[1]Dipartimento di Ingegneria, Università degli Studi di Palermo, Viale delle Scienze, Palermo, Italy

[2]Dipartimento di Biomedicina, Neuroscienze e Diagnostica avanzata (Bind), Università degli Studi di Palermo, Palermo, Italy

[3]Dipartimento di Scienze Biomediche, Istituto per la Ricerca e l'Innovazione Biomedica, CNR, via U. La Malfa 153, Palermo, Italy

[4]Dipartimento di Scienze e Tecnologie Biologiche Chimiche e Farmaceutiche, Università di Palermo, Viale delle Scienze, Palermo, Italy

Correspondence: Pasquale Picone (pasquale.picone@cnr.it) | Francesco Lopresti (francesco.lopresti01@unipa.it)

Domenico Nuzzo and Vincenzo La Carruba are the co-last authors.

Funding information
MUR PNRR; European Union – NextGenerationEU

Abstract

A major challenge in pharmacology is the limited selectivity of therapeutic compounds toward specific tissues or cells. Drugs often distribute systemically before reaching the intended site of action, affecting nontarget cells and potentially reducing efficacy or causing side effects. Traditional two-dimensional cultures fail to reproduce the three-dimensional architecture and dynamic microenvironment of tissues. Here, we present a novel microfluidic platform integrating an electrospun scaffold to assess the selective interaction of drugs or nanosystems with different central nervous system (CNS) cell types as model. The device was engineered to enable the coculture of two distinct cell types in separated compartments that remain fluidically connected, thus simulating physiological exposure and transport conditions. This setup allows for dynamic testing of compound selectivity in a more relevant context. Overall, this integrated and modular system represents a promising tool for advancing in vitro brain models and improving the predictive power of preclinical drug screening strategies targeting the CNS.

KEYWORDS

brain on chip, cell-specific drug selectivity, electrospun scaffold, microfluidic device, nanosystems

Maria Testa and Laura Palumbo contributed equally to this work.

1 | INTRODUCTION

Assessing compound selectivity is essential for the development of novel therapeutics and repositioning of existing drugs for alternative applications.[1] One of the major challenge associated with conventional drug delivery strategies is their limited selectivity in targeting particular tissues and cells.[2] Therapeutic compounds often disperse systemically before reaching the intended site of action, potentially exerting effects, not always beneficial, on non-target cells.[3] Therefore, reliable in vitro models capable of predicting drug selectivity at an early stage are urgently needed. Such platforms would not only reduce the reliance on animal models, which often fail to capture human-specific responses, but also accelerate the identification of compounds with favorable therapeutic indexes.[4] The traditional static in vitro methods such as multiwell plates fail to reproduce the intricate physiological environment of human organs. These simplified systems are also unable to reproduce the physiological gradients of nutrients, signaling molecules, and oxygen that naturally arise in tissues and vary with their volume and structure.[5] Moreover, they lack the ability to mimic key features such as tissue-specific organization, mechanical and biochemical cues, and the intricate network of cell–cell and cell–extracellular matrix (ECM) interactions.[6] To better replicate the physiological dynamic flow conditions, the organ-on-chip (OoC) approach was developed. This technology employs miniaturized microfluidic devices, which incorporate networks of microchambers and microchannels to sustain laminar flow and support cell culture under conditions that closely resemble the in vivo setting.[7] The core principle behind OoC systems is to recreate the functional responses of specific cell types under flow, allowing for the investigation of both physiological and pathological processes.[4] OoC devices can be equipped with scaffolding materials composed from natural or artificial matrices that can mimic the ECM of the in vivo microenvironment providing cells with a biomimetic niche that instructs cell fate in a similar way to the native ECM, thus allowing the recapitulation of complex processes.[8] Among the different scaffolding systems electrospun (ES) materials have gained increasing traction in neural tissue engineering due to their ability to mimic the structural and biochemical characteristics of the native ECM.[9] These scaffolds provide aligned or random topographical cues that influence cellular orientation, elongation, and directional migration, promoting physiologically relevant cell behavior.[10] Wang et al. demonstrated that Schwann cell migration and elongation are highly dependent on fiber diameter and alignment, with maximal migration observed on aligned fibers of approximately 1.3 μm in diameter (1325 ± 383 nm).[11] Beyond glial behavior, electrospinning has also been employed to guide neurite outgrowth and support the generation of other neural tissue structures.[12] Despite the clear benefits, only a limited number of OoC platforms currently incorporate ES membranes, missing the opportunity to merge the biologically relevant architecture of fibrous scaffolds with the precise spatial and fluidic control provided by microfluidic technologies.[7, 13–17] Moreover, although various OoC and multi-OoC systems have been developed to study pharmacokinetics parameters such as drug absorption, distribution, metabolism, and excretion,[18] no platform to date has been specifically designed to evaluate drug selectivity across different cell populations in a microfluidic controlled system. In this article, a microfluidic device was specifically designed to support the coculture of two distinct cell types in spatially isolated compartments, yet within a shared fluidic environment, enabling the investigation of selective drug–cell interactions under conditions that closely resemble physiological settings. Unlike traditional polydimethylsiloxane (PDMS)-based systems, this platform was developed using thermoplastic polymers combined with rapid prototyping methods to improve scalability and manufacturability.[19] A key focus of the design was the integration of a septum ensuring separation between the two culture chambers during the seeding step. Additionally, computational fluid dynamics (CFD) simulations were employed to optimize the flow characteristics, confirming that the system sustains fluid velocities within physiologically relevant values.

As a proof of concept, the developed microfluidic device was employed to establish a simplified yet representative model of the central nervous system (CNS). Specifically, neural cells (SH-SY5Y), together with microglial cells (BV2), were cocultured in the two spatially separated compartments of the chip while sharing the same fluidic environment during the perfusion step. To assess the potential of the platform in evaluating selective drug–cell interactions, we investigated the effects of a nanovesicle-based formulation[20, 21] as a model therapeutic compound. This approach demonstrated the capability of the system to sustain cell viability under flow and to provide measurable readouts of compound selectivity across different CNS-relevant cell populations when perfused at physiological interstitial velocities. In conclusion, this study aims to address one of the most significant challenges in preclinical pharmacology: the difficulty of assessing drug selectivity toward a specific cell type in vitro. This study presents, for the first time, a pioneering microfluidic platform integrating an ES scaffold, purpose-built to assess the selective interaction of drugs or drugs delivery systems with distinct CNS cell types. This approach not only allows for a three-dimensional in vitro model, thanks to the ability

of cells to colonize and entangle within the ES membranes but also recreates a dynamic physiological microenvironment of cellular interaction, in which released metabolites can pass from one chamber to another even in the absence of direct cell–cell contact. Furthermore, the presence of a flow, capable of reproducing fluid velocities representative of interstitial fluid flow with greater realism than a static system, represents a crucial element, since it allows for the evaluation of the real specificity and selectivity of the interaction of the drug or delivery system, significantly reducing nonspecific interactions. Furthermore, this system is modular, as it can be designed to contain more than two cell lines in the same microenvironment by incorporating additional separation septa. Finally, the system represents a rapid and efficient screening platform, as it is compatible with simple fluorescent detection methods such as direct scanning or microscopy, without the need for cell fixation.

2 | MATERIALS AND METHODS

2.1 | Materials

Poly(lactic acid) (grade 2002D; NatureWorks, Minnetonka, MN, USA) was selected as the base material for scaffold production. PLA was dissolved using a solvent mixture composed of acetone (Ac) and chloroform (TCM), both obtained from Sigma–Aldrich (Saint Louis, MO, USA). For the fabrication of the brain-on-chip (microfluidic platform) devices, polymethyl methacrylate (PMMA) sheets of various thicknesses (Clarex; Nitto Jushi Kogyo Co. Ltd., Tokyo, Japan) were utilized, supplied by Weatherall Ltd (Wendover, UK).

2.2 | ES scaffold fabrication

PLA-based solutions for electrospinning were obtained by dissolving the polymer at a concentration of 10 wt% in a TCM:Ac (2:1 v/v) mixture. The dissolution process was carried out at room temperature under continuous magnetic stirring and left overnight to ensure full homogenization. The resulting solution was loaded into a 10 mL glass syringe equipped with a 20-gauge stainless steel needle. Electrospinning was performed using a NF-103 apparatus (MECC Co., Ltd., Fukuoka, Japan), with operating parameters derived from previously optimized settings.[22] Specifically, the flow rate of the solution was maintained at 0.7 mL/h, with an applied voltage of 17 kV and a fixed needle-to-collector distance of 20 cm. To enhance uniformity in fiber deposition, the needle was programmed to oscillate along the *x*-axis over an 8 cm span at a speed of 10 mm/min. The collector consisted of a grounded rotating drum (10 cm in length, 10 cm in diameter) operating at 100 rpm for the fabrication of scaffolds composed of random fibers (R-PLA) while it was set at 4000 rpm for the fabrication of scaffolds composed of aligned fibers (A-PLA), covered with aluminum foil to facilitate scaffold removal. The electrospinning process was carried out for 300 min to produce fibrous mats approximately 15 × 20 cm in size and ∼80 μm in thickness in the case of R-PLA and ∼50 μm in the case of A-PLA samples. Postprocessing, the collected samples were dried for 48 h under a fume hood to eliminate residual solvents.

2.3 | Microfluidic platform design and fabrication

The design of the microfluidic system and its components was carried out using Autodesk Fusion 360™ (Autodesk, San Rafael, CA, USA). The microfluidic platform was specifically designed to compartmentalize two distinct cell populations in separate regions of the device, allowing them to interact within a shared culture volume under dynamic flow conditions. This configuration enables the assessment of drug selectivity by recreating a controlled microenvironment where intercellular communication and pharmacological responses can be closely monitored. The entire device was modeled in 3D CAD and structured into four functional layers, each characterized by a defined thickness and function. To fabricate these layers, the 3D model was digitally sliced into individual 2D geometries (Figure S1), which were then converted from STL to DXF format to enable compatibility with the laser micromachining software.

Fabrication was performed using a CO_2 laser cutting system (Maitech; 40 W, Milan, Italy) mounted on a stage with adjustable *z*-height, enabling high-precision processing of both polymethyl methacrylate (PMMA) substrates and ES scaffolds.[19, 23] Cutting and engraving were guided by the computer-generated vector paths at a focal distance of 2.1 cm. For the fabrication of the layers, laser processing parameters were optimized to ensure precision and reproducibility. Cutting operations were performed with a laser power of 30% and a speed of 15 mm/s, while engraving steps were carried out using a power of 35% and a speed of 200 mm/s. For the ES membrane, lower energy settings were applied to avoid damaging the fibrous structure, with engraving conducted at 5% laser power and 270 mm/s speed. Following laser processing, each PMMA layer was immersed in a 70:30 vol mixture of water and ethanol and subjected to ultrasonic cleaning for 3 min to eliminate PMMA dust residues. Posttreatment with Trichloromethane, chloroform (TCM) vapor for 3 min was performed on the engraved PMMA layers to restore optical transparency.

The cleaned PMMA layers were aligned using custom-fabricated aluminum alignment plates equipped with metal pins, with ethanol applied on the contact surface to improve the bonding efficiency.[19, 23] The ES scaffold was carefully positioned in the designated region of the multilayer stack. Final bonding was achieved by applying 70°C and 100 bar pressure for 3 min using a laboratory-grade hot press (Carver Laboratory Press, Fred S. Carver, Inc., Menominee Falls, WI).[16]

2.4 | CFD analysis

CFD simulations were performed on the culture chambers of the microfluidic device using ANSYS Fluent Academic Edition 2025R2 (Analysis Systems Inc.). The incompressible Navier–Stokes and continuity equations were solved using the finite volume method under laminar flow conditions. A tetrahedral mesh with local refinement at the cell–substrate interfaces was employed to ensure accurate resolution of near-wall gradients. For perfusion analysis, a steady-state pressure-based solver with SIMPLEC velocity–pressure coupling was used.

To evaluate oxygen availability, a transport of diluted species model was implemented in both static and dynamic configurations, including oxygen diffusion in the culture medium ($D = 2 \times 10^{-9}$ m^2/s, 37°C) and convective effects only during perfusion. The inlet concentration was set to 0.194 mM, consistent with equilibrated culture medium under standard incubator conditions (100% humidity, 5% CO_2).[24] Oxygen consumption by cells was applied as a boundary sink at the fluid–cell interface, using literature-based uptake rates (3.33 nM/10^6 cells/min for BV2 microglial cells[25] and 2.5 nM/10^6 cells/min for SH-SY5Y neuroblastoma cell[26]) and the seeding densities used experimentally. Considering initial seeding densities of 6×10^4 BV2 cells and 12×10^4 SH-SY5Y cells per compartment (0.26 cm^2 each), the total cellular oxygen uptake was estimated to be $\sim 1.45 \times 10^{-10}$ kmol/(m^2 s) and $\sim 2.18 \times 10^{-10}$ kmol/(m^2 s) for BV2 and SH-SY5Y, respectively.

Static culture (24 h postseeding) was reproduced using a transient PISO solver and a volume of fluid model to describe the air–liquid interface. Henry's law equilibrium was imposed to allow oxygen transfer from the air headspace into the medium, while convection was suppressed within the liquid phase. Oxygen concentration maps were extracted to identify potential hypoxic regions and validate the device design in maintaining physiological oxygen levels in both culture compartments.

2.5 | Porosity measurement

The porosity (φ) of the A-PLA and R-PLA scaffolds was evaluated using the following Equation (1)[27]:

$$\varphi = 1 - \frac{\rho_{\text{scaffold}}}{\rho_{\text{PLA}}} \tag{1}$$

where ρ_{scaffold} refers to the apparent density of the scaffold and ρ_{PLA} is the density of the bulk PLA material, as provided by the supplier's technical datasheet. The resulting value of φ is a dimensionless quantity that represents the scaffold's porosity that was reported in percentage.

For this analysis, five ($N = 5$) scaffolds were cut into circular shapes of defined diameter using a laser cutter. Their masses were measured with a high-precision analytical balance, while their volumes were determined based on their known dimensions. The apparent density of each scaffold was then calculated using the following Equation (2):

$$\rho_{\text{scaffold}} = \frac{M_{\text{scaffold}}}{V_{\text{scaffold}}} \tag{2}$$

2.6 | Cells culture

SH-SY5Y cells, generously provided by Dr Venera Cardile of the University of Catania, were cultured in T75 tissue culture flasks in Dulbecco's modified Eagle medium/nutrient mixture F-12 (DMEM/F12) (Thermofisher) supplemented with 10% fetal bovine serum (FBS) (GIBCO Invitrogen, Milan, Italy) and 100 U/mL penicillin and 100 U/mL streptomycin.BV2 microglial cells were cultured in T25 high-glucose DMEM (Thermofisher) supplemented with 10% FBS (Gibco), 100 U/mL penicillin, 100 U/mL streptomycin, and 2 mM L-glutamine.

2.7 | Insert preparation for evaluating cell growth under static conditions

To test the biocompatibility of the fibers under static conditions, inserts with a comparable diameter to that of the 96-well plates were used. These inserts featured either aligned or random membranes. Prior to seeding, the inserts were sterilized by placing them in a 70% ethanol solution for 2 h, followed by sterilization under UV light for 20 min on both sides. Once dry, the inserts were placed in a 48-well plate ready for cell seeding.

2.8 | Cell viability and cytotoxicity assays in static conditions

Cell viability was measured using the MTS assay (Promega). MTS [3-(4,5-dimethylthiazol-2-yl)-5-(3-carboxymethoxyphenyl)-2-(4-sulfophenyl)-2H-tetrazolium] was used according to the datasheet protocol. Bv2 cells and SH-SY5Y cells were seeded in triplicate into inserts with random or aligned fibers. The different seeding densities used for BV2 and SH-SY5Y cells of 6×10^{-4} and 12×10^{-4} cells/chamber, respectively, is due to the different replication rates of the cells. Twenty-four hours after seeding, 20 µL of the MTS solution was added to each well containing the cells and incubated for 4 h at 37°C, 5% CO_2. Absorbance was read at 490 nm using a Glomax microplate reader (Promega). Values are compared with culture medium values. At the same time, to confirm the presence of cells on the fibers and their ability to support cell adhesion and growth, cells were plated at the same concentration and for the same period of time and incubated with Hoechst 33342 trihydrochloride trihydrate for nuclear staining. Cells were then observed with an IX83 fluorescence microscope (Evident/Olympus) at 20× magnification.

2.9 | Immunostaining and microscopy in static conditions

Twenty-four hours after seeding, BV2 and SH-SY5Y cells were fixed with 4% paraformaldehyde (PFA) for 15 min and permeabilized with 0.1% Triton X-100 in PBS for 10 min at room temperature. Subsequently, they were blocked with 2% BSA at room temperature for 1 h and incubated with primary antibodies to β-tubulin III (c.s 5568s), ionized calcium-binding adapter molecule 1 (IBA1) (c.s 17198s) overnight at 4°C in a humidified chamber. Subsequently, incubation with secondary antibodies conjugated with Alexa Fluor 546 (1:1000) (IBA1 and β-tubulin III) was performed for 1 h in the dark at room temperature. Finally, the cells were washed with PBS and stained with DAPI (1 µg/mL) for 7 min in the dark at room temperature. Fluorescence imaging was performed with the IX83 fluorescence microscope (Evident/Olympus) at a magnification of 20×.

2.10 | Brain on chip preparation for cell growth in dynamic condition

To perform studies under dynamic conditions, microfluidic platform chips featuring either aligned or random membranes were used. Before seeding, the chips were sterilized by placing them in a 70% ethanol solution for 2 h and then sterilized under UV light for 20 min. After allowing the chips to dry, 6×10^{-4} cells/chamber of BV2 and 12×10^{-4} cells/chamber of SH-SY5Y were plated.

2.11 | Myelin nanovesicles production and functionalization

Myelin nanovesicles (MyVes) were prepared using a nanoprecipitation method as previously described.[20, 21] Briefly, myelin extract was dissolved inDimethyl sulfoxide (DMSO) at a concentration of 2 mg/mL and sonicated for 30 min at 35 kHz. Subsequently, this solution was added dropwise ultrapure water (volume ratio DMSO/water 1:20) under vigorous agitation using an ultraturrax homogenizer (600 g, 15 min). The resulting suspension was purified by repeated ultracentrifugation (30 min at 340.000 g), redispersed in ultrapure water, and then freeze-dried. Fluorescently labeled MyVes were obtained from the freeze-dried nanovesicles. The lyophilized MyVes were redispersed in Dulbecco's phosphate-buffered saline (DPBS pH 7.4) at a concentration of 2 mg/mL. To this dispersion, 50 µL of Atto 633 NHS ester in DMSO (2 mg/mL) was added. The mixture was incubated for 2 h in the dark to allow for conjugation, followed by ultracentrifugation (30 min at 50,000 rpm). The vesicles (MyVes-Atto633) were then washed three times with ultrapure water, each followed by ultracentrifugation under the same conditions. Finally, the fluorescent MyVes were redispersed in 2 mL of ultrapure water and freeze-dried.

2.12 | Brain on chip treatment with MyVes-Atto633 and fluorescence analysis

Twenty-four hours after seeding, the cells in the chip were treated with a 30 µg/mL MyVes-Atto633 solution in the culture medium. The pump flow was started at a rate of 1.39 mL/h for 2 h. The cells were then washed in DPBS and stained with Hoechst to detect nuclei. Fluorescence was first detected using a Typhoon FLA 9500 and then using with the IX83 fluorescence microscope (Evident/Olympus) at a magnification of 4×.

2.13 | Morphological characterization

The morphological characterization of the fibrous scaffolds and the evaluation of cell attachment were carried out using a scanning electron microscope (SEM; Quanta 200 F, FEI, USA). Circular sections of the samples (Ø 3 mm) were mounted on aluminum stubs using conductive carbon adhesive. Prior to imaging, specimens were sputter-coated with a thin layer of gold (Sputtering Scancoat Six, Edwards Laboratories, Milpitas, CA, USA) for

120 s under an argon atmosphere to enhance conductivity and image resolution. SEM analysis was performed also on scaffolds retrieved from the microfluidic platform system after dynamic cell culture experiments.

Scaffolds previously used for cell culture were processed for fixation and dehydration prior to SEM analysis. Samples were fixed in a 4% (v/v) PFA in DPBS at room temperature for 30 min. The fixation step was followed by a dehydration process using a graded series of ethanol–water mixtures, increasing in ethanol concentration, as described in prior protocols.[28]

Images were acquired at multiple time points to monitor cell adhesion, spreading, and scaffold colonization over time. Fiber diameter and angular distribution was quantitatively assessed using DiameterJ and OrientationJ plugin integrated into the ImageJ software suite.[29] Fiber alignment was quantified from angular distribution histograms by calculating the mean fiber orientation and the standard deviation of angular dispersion. In addition, an alignment index was computed to quantify the degree of orientational order. This index was defined as the average second-order cosine of the fiber orientation angle, $\langle \cos^2\theta \rangle$, where θ is the angle of the fiber to the x axis, according to Bernasconi et al.[30]

For cellular orientation distribution, SEM images were processed to isolate cellular contours using edge enhancement and intensity thresholding. The resulting binary masks were used to perform angular orientation analysis using the OrientationJ plugin. Angular distributions were computed with the finite difference gradient analysis mode within a defined region of interest to avoid areas dominated by scaffold fibers. The relative frequency (%) of cell orientation was calculated for angular bins ranging from −90° to +90°. Orientation distribution graphs were generated for each condition to compare directional organization across substrates and cell types. Three independent images per condition were analyzed, and peak angular frequencies were extracted as a metric of preferred alignment. Lower angular dispersion was interpreted as increased cellular alignment along a preferential axis. The overall microfluidic chip morphology and layer alignment of the microfluidic platform device were inspected using a Dino-Lite digital microscope (Model AM4115T-CFVW; Dino-Lite, Almere, The Netherlands).

3 | RESULTS AND DISCUSSIONS

3.1 | Microfluidic platform design and rationale of use

The microfluidic platform was designed to evaluate the selectivity of pharmacological compounds toward distinct cell populations cultured within a shared, perfused environment. Each microfluidic device integrates two identical culture chambers, allowing parallel experiments to be performed under identical fluidic conditions within the same platform. Each culture chamber enables direct comparison of drug selectivity on two different cell types. The system enables direct comparison of compound–cell interactions by allowing two different cell types to be initially spatially segregated and subsequently exposed to the same culture medium under controlled flow conditions, mimicking physiologically relevant interstitial fluid velocities.

As illustrated in Figure 1A each culture chamber consists of a single culture chamber in which two symmetrical regions are defined by a central septum. The chamber has a total height of 4 mm, while the septum is 2 mm high and deliberately lower than the chamber ceiling. This design ensures that, upon perfusion, the culture medium can overflow the septum, creating controlled communication between the two compartments within a unified fluidic environment.

An ES scaffold is fixed to the bottom of the culture chamber as substrate for cell adhesion; therefore, cells are directly exposed to the culture medium and any supplemented drug or drug delivery systems. Accordingly, the ES scaffold does not act as a transport interface or diffusion barrier between distinct fluidic compartments, but solely as a biomimetic substrate providing topographical cues for cell adhesion and survival.

For comparative purposes, scaffolds composed of either randomly oriented or aligned fibers were employed to investigate the influence of substrate architecture on cellular behavior.

Each culture chamber includes three inlet channels and one outlet (Figure 1A). The two lateral inlets are used to independently seed BV2 (microglial) and SH-SY5Y (neuronal) cells into the respective regions, which remain physically separated during the initial seeding phase. Following cell seeding, the lateral inlets are sealed, and the central inlet is used to introduce culture medium or drug-containing medium, which fills the entire chamber and enables interaction between the previously segregated cell populations under dynamic conditions.

The outlet is located at the bottom of the chamber to ensure efficient medium exchange and to maintain continuous contact between the perfused solution and the cell layer adhered to the scaffold. This configuration also helps to prevent the accumulation of the drug within the culture chamber, ensuring a more controlled and reproducible exposure profile.

Figure 1B illustrates the microfluidic platform device in its exploded view, highlighting the four functional layers (L1–L4) that compose its architecture. Each layer is designed to be fabricated from PMMA preformed

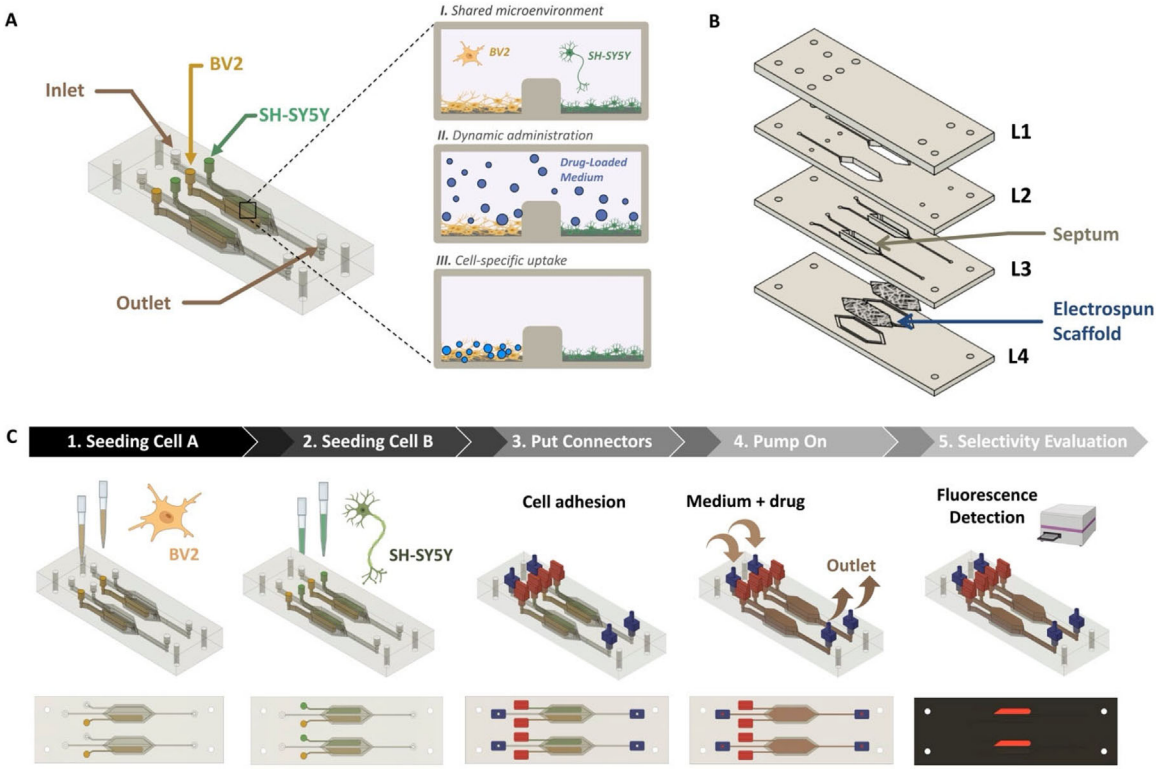

FIGURE 1 Overview of the microfluidic platform design, architecture, and experimental workflow. (A) Conceptual schematic representation of the single-chamber microfluidic platform illustrating the shared perfused microenvironment. Two distinct cell populations (Cell A and Cell B) are cultured on an ES scaffold positioned at the bottom of the chamber and exposed to the same dynamically perfused medium. The system enables the administration of drugs or drug delivery systems and the evaluation of cell-type-specific uptake within a unified fluidic environment. (B) Exploded view of the multilayer thermoplastic architecture of the device (L1–L4), highlighting the presence of the septum and the integration ES scaffold at the base of the culture chamber. (C) Experimental workflow of the platform, including sequential seeding of the two cell populations, a static adhesion phase, dynamic perfusion with drug or drug delivery systems containing medium, and fluorescence-based readout for the assessment of selective uptake.

sheets with specific thicknesses by means of laser cutting/engraving to produce the microstructures meant to fulfill distinct roles within the device. Layer 1 (L1), with a thickness of 3 mm, is dedicated to housing the inlet/outlet ports. It includes circular holes to accommodate microfluidic connectors or sealing caps, enabling both fluid delivery and modular closure of the chamber system. Layer 2 (L2), 2 mm thick, contains the microchannel for directing the flow of the culture medium into the central culture chamber. Its geometry ensures even distribution across the chamber volume. Layer 3 (L3), 2 mm thick, incorporates the microchannels used for the independent seeding of the two cell populations. This layer also includes the septum that physically divides the culture chamber into two symmetrical compartments during the initial seeding phase. Additionally, L3 features the outlet channel, positioned at the bottom of the chamber to facilitate circulation of the perfused medium.

Layer 4 (L4) contains an engraved recess specifically designed for precise placement of the ES scaffold. This layer anchors the fibrous substrate at the base of the culture chamber, providing a biomimetic surface for cell adhesion and growth.

Figure 1C schematically illustrates the working principle of the microfluidic platform device applied to the biological system used in this study as proof of concept. In this experimental setup, BV2 (microglia) and SH-SY5Y (neurons) are selectively seeded into two separate regions of the culture chamber (Steps 1 and 2). Following cell seeding, microfluidic connectors (shown in blue) are inserted into the central inlet and outlet ports to enable perfusion, while the lateral inlet ports, used only for seeding, are sealed with appropriate plugs (red). A static incubation period of 24 h is then allowed for cell adhesion onto the ES PLA scaffold, composed of either R-PLA or A-PLA fibers (Step 3). In Step 4, a drug-containing medium is introduced and perfused for 2 h, establishing the conditions for selective stimulation of the cultured cells. In Step 5, drug selectivity is assessed by means of a fluorescent marker used either as a label or as a reporter of drug uptake.

Due to the high optical transparency and low autofluorescence of PMMA, fluorescence microscopy and/or

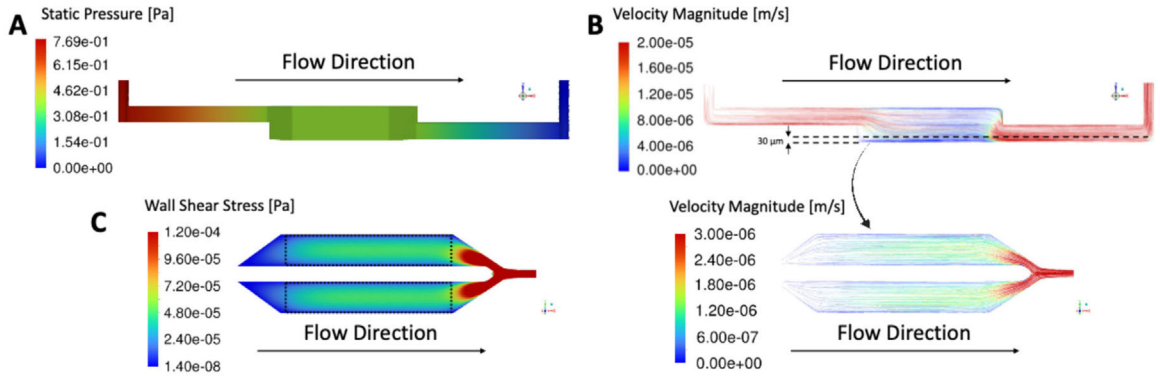

FIGURE 2 Computational fluid dynamics (CFD) simulation results for the microfluidic platform device. (A) Simulated pressure drops across the device under a flow rate of 1.39 mL/h. (B) Flow streamlines visualized in both lateral and top views. (C) Wall shear stress distribution at the culture surface.

fluorescence scanner can be effectively employed to detect the presence and localization of the marker. A selective drug would produce a fluorescent signal only in the compartment containing responsive cells, while the other region would remain unstained, thus confirming selective targeting.

To select the appropriate flow rates for perfusing the medium, a CFD analysis was performed on the fluid volume (Figure 2A–C). The goal was to achieve fluid velocities near the cell culture surface comparable to those typically found in interstitial brain tissue (ranging from 0.1 to 1.0 µm/s in normal tissues[31]). A trial-and-error approach was used, testing different flow rates until the optimal one was identified, set at 1.39 mL/h.

The evaluation of drug selectivity under physiologically relevant velocities provides a more realistic assessment compared with static cultures. In vivo, compounds are transported within a constantly perfused environment, where the interplay between fluid velocity, concentration gradients, and continuous renewal of the medium critically influences both their diffusion dynamics and their interaction with cellular barriers. Static conditions, in contrast, often lead to nonphysiological accumulation or depletion of compounds in the pericellular space, generating artificial gradients that may overestimate or underestimate selectivity values. By perfusing the system at velocities within the physiological range, our platform better reproduces the convective and diffusive mechanisms naturally occurring in tissues, ensuring that drug distribution and subsequent uptake reflect in vivo-like kinetics. This is particularly relevant for assessing selectivity, as the exposure of different cell types to a continuously refreshed compound reservoir reduces the risk of artifacts due to nonspecific binding or prolonged static contact.[32–34]

Figure 2A shows the results of the pressure drop across the device when a flow rate of 1.39 mL/h is applied. The calculated pressure drop across the device is approximately 0.8 Pa, indicating negligible pressure-related effects under the investigated operating conditions. Figure 2B displays the flow streamlines throughout the device in a lateral and top view, with the arrow indicating the flow direction. Due to the inlet being positioned at the top and the outlet at the bottom, the design promotes a diagonal flow path across the culture chamber. As expected, higher velocities are observed in the inlet channels, followed by a sharp decrease within the culture chamber due to the increased cross-sectional area. The top-to-bottom flow pattern minimizes the risk of drug accumulation or stagnant regions, reducing potential assay bias.

The zoomed-in top-view highlights the velocity pathlines at a height of 30 µm from the chamber base, corresponding to the region of direct interaction between the perfused medium (and drug) and the adherent cells. This view reveals a fairly uniform velocity distribution across the chamber, excluding inlet and outlet regions. The velocities evaluated at 30 µm from the cell culture surface are within the physiological range (0.29–1.45 µm/s), confirming the device's ability to replicate in vivo-like interstitial fluid velocity.

The shear stress map in Figure 2C reports values ranging from 1.2×10^{-4} to 1.2×10^{-3} dyne/cm^2.[31] Notably, the central rectangular region highlighted in the figure exhibits a highly uniform wall shear stress distribution, with an average value of approximately 6×10^{-4} dyne/cm^2 and was therefore selected for quantitative analysis.

Furthermore, to verify whether the selected perfusion conditions ensure an adequate oxygen supply to both cell populations, a CFD analysis of oxygen transport and cellular consumption was conducted.

Under dynamic perfusion conditions, the inlet mass fraction of dissolved oxygen was set to 6.4×10^{-6} w/w, corresponding to a concentration of 0.194 mol/m^3, consistent with equilibrated culture medium under standard incubator conditions.[24] As shown in Figure 3, oxygen

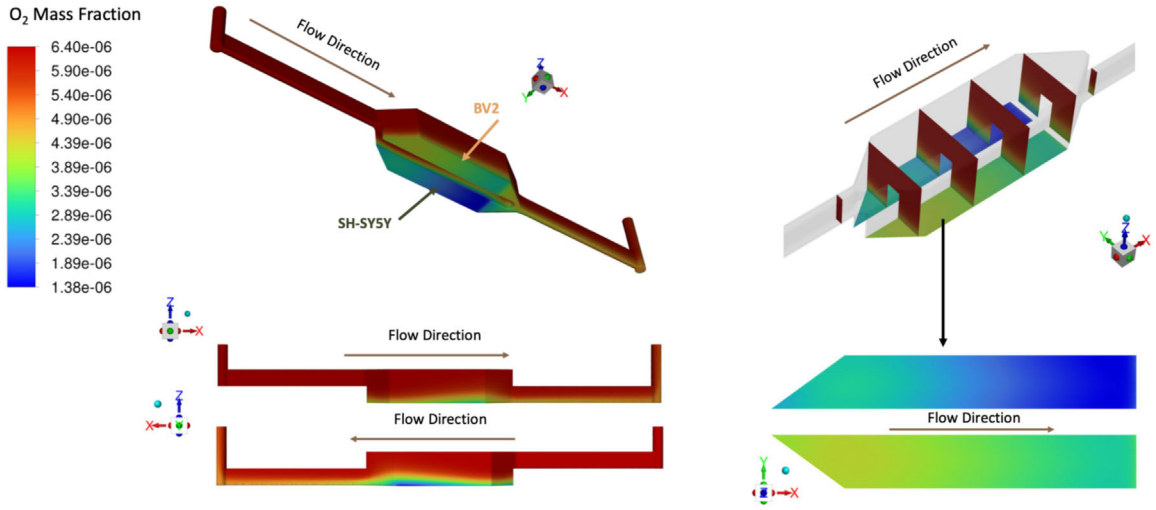

FIGURE 3 CFD simulation under dynamic perfusion. Oxygen mass fraction distribution within the fluid domain, visualized from different perspectives.

was progressively consumed by adherent cells along the flow direction in both compartments, resulting in a modest decrease in oxygen concentration at the outlet, where the oxygen mass fraction reached 5.9×10^{-6} w/w, corresponding to approximately about 92% of the inlet value. The strongest depletion was observed in the SH-SY5Y compartment, which hosts the higher cell number and exhibits the higher specific oxygen uptake rate. In this region, the minimum oxygen mass fraction at the cell layer dropped to 1.38×10^{-6} w/w, that is, about 22% of the inlet value, in the area closest to the outlet. In the BV2 compartment, the minimum O_2 mass fraction was higher, 3.0×10^{-6} w/w (about 47% of the inlet value). When oxygen concentrations predicted by the CFD model were compared against the metabolic thresholds of both cell populations, the minimum values within the culture regions remained consistently above the respective Michaelis–Menten constants. In particular, the reported K_m values for oxygen uptake are 0.7×10^{-3} mol/m^3 (2.24×10^{-8} w/w) and 2.97×10^{-3} mol/m^3 (9.50×10^{-8} w/w) for SH-SY5Y[35] and BV2[36] cells, respectively, thus two order of magnitude lower than the corresponding minimum oxygen mass fraction predicted by the simulation. This indicates that cellular oxygen consumption remains in a near zero-order kinetic regime and oxygen availability is not a limiting factor for metabolism. Overall, CFD analysis confirms that the perfusion strategy adopted in the device ensures adequate oxygenation for both neuronal and microglial populations throughout the entire culture chamber.

Simulations were also carried out to evaluate oxygen availability in the absence of perfusion to emulate static seeding phase (Figure 1C, Step 3). As the chamber is not completely filled with medium, a ~2 mm air headspace remains above the culture surface, functioning as a local oxygen reservoir that enables passive oxygen replenishment through diffusion across the air–liquid interface according to Henry's law. At the beginning of the simulation (0 h), the culture medium was fully oxygenated, with an oxygen mass fraction equal to 6.4×10^{-6} w/w. Due to cellular uptake, oxygen gradually decreased along the culture surface over time, with lower concentrations near the cell layer and higher values toward the air–liquid interface (Figure 4). In the BV2 compartment, the minimum oxygen mass fraction reached 4.10×10^{-6} w/w after 2 h, 3.04×10^{-6} w/w after 4 h, and 2.14×10^{-6} after 24 h w/w. As expected, the SH-SY5Y compartment exhibited stronger depletion due to higher cell number, with minimum mass fraction values equal to 2.99×10^{-6} after 2 h, 1.56×10^{-6} after 6 h, and 1.02×10^{-6} after 24 h. Similarly to the dynamic condition, oxygen availability remained well above the metabolic threshold (K_m) for both cell populations throughout the static phase. Although oxygen depletion progressed over time, the air pocket above the culture medium acted as a reservoir that continuously replenished dissolved oxygen, preventing critical drops near the cell layer. As a result, no hypoxic zones were generated, and cellular consumption continued operating under oxygen-saturated conditions.

3.2 | Microfluidic platform fabrication and scaffold morphology

PMMA is well suited for micromachining via laser cutting and engraving, enabling the fabrication of functional layers with an adequate level of definition for microfluidic applications.[19] As shown in Figure 5A, the four functional layers (L1–L4) were obtained through laser cutting

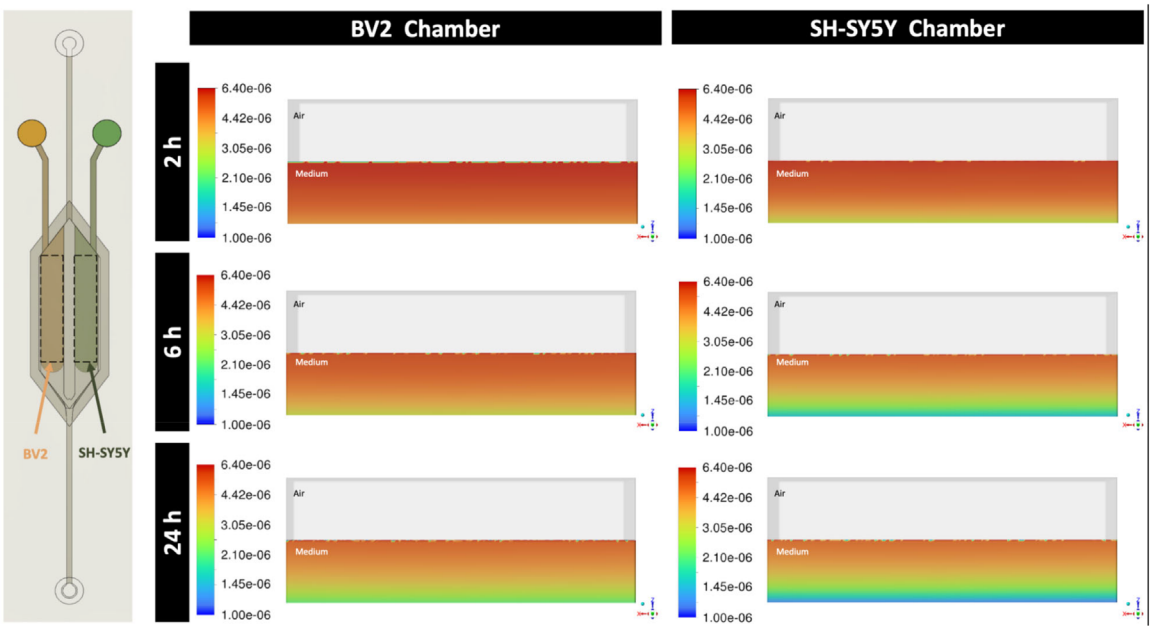

FIGURE 4 CFD analysis reporting the oxygen mass fraction distribution during static culture of BV2 and SH-SY5Y cells after 2, 6, and 24 h from seeding. The chamber is only partially filled with medium, leaving about 2 mm air headspace that acts as a local oxygen source.

and engraving. The resulting structures closely match the design specifications shown in Figures 1B and S1. Notably, in layer L3, the central septum separating the two culture chambers remains straight and undeformed by the processing steps, demonstrating the precision achievable with this method. To ensure this outcome, a preliminary study was conducted to evaluate the minimum viable thickness of septum. This optimization step led to the identification of 2 mm as the minimum width necessary to maintain structural integrity without warping during laser processing. Layer L4 also clearly displays the engraved regions designed to accommodate and anchor the ES scaffold.

Proper cleaning of the PMMA layers after laser ablation is a critical step in the fabrication of microfluidic devices, as it prevents clogging and ensures consistent functionality.[37] Laser ablation is known to generate debris, particularly in PMMA, due to the recondensation of the vaporized polymer during processing. For layers processed only by laser cutting, this effect is minimal, and a standard ultrasonic bath in 70:30 ethanol:water solution is generally sufficient to remove the resulting particles.[19] However, in the presence of engraved regions, the risk of particle accumulation is significantly higher. For this reason, the cleaning protocol for L4, which contains an engraved region, included an additional step involving TCM vapor treatment to eliminate residual PMMA debris. As shown in Figure 5B, the engraved region of L4 appears whitish and significantly less transparent than the surrounding surface. SEM analysis of the laser-exposed area revealed a combination of micropores and particles, consistent with typical laser ablation artifacts and explaining the observed opacity. Following the ultrasonic cleaning step in ethanol (Figure 5C), the surface appeared macroscopically similar; however, SEM images showed a significant reduction in the number of particles, although pores ranging from a few micrometers to tens of micrometers in diameter remained. After TCM vapor treatment (Figure 5D), the engraved surface appeared markedly more transparent, allowing clear visualization of the black background beneath it. SEM images confirmed that the surface was free of both particulate matter and the porosity induced by the laser ablation, resulting in a smooth and homogeneous morphology, except for the presence of occasional microcracks.

Figure 6A shows the device after the assembly process. The image qualitatively highlights the overall build quality of the chip, with well-aligned layers ensured using corner alignment holes and integrated alignment pins into the mold.

Figure 6B depicts a representative step of the cell seeding procedure. Two aqueous solutions, each containing a different food dye, were introduced into the two separate compartments of the culture chamber to simulate the seeding of two distinct cell suspensions. A volume of 80 µL was injected into each compartment.

A magnified view of the terminal region of the culture chamber, acquired using a digital microscope and presented in Figure 6C, illustrates that the inserted volumes fully cover the respective culture surfaces without any cross-contamination between compartments. These

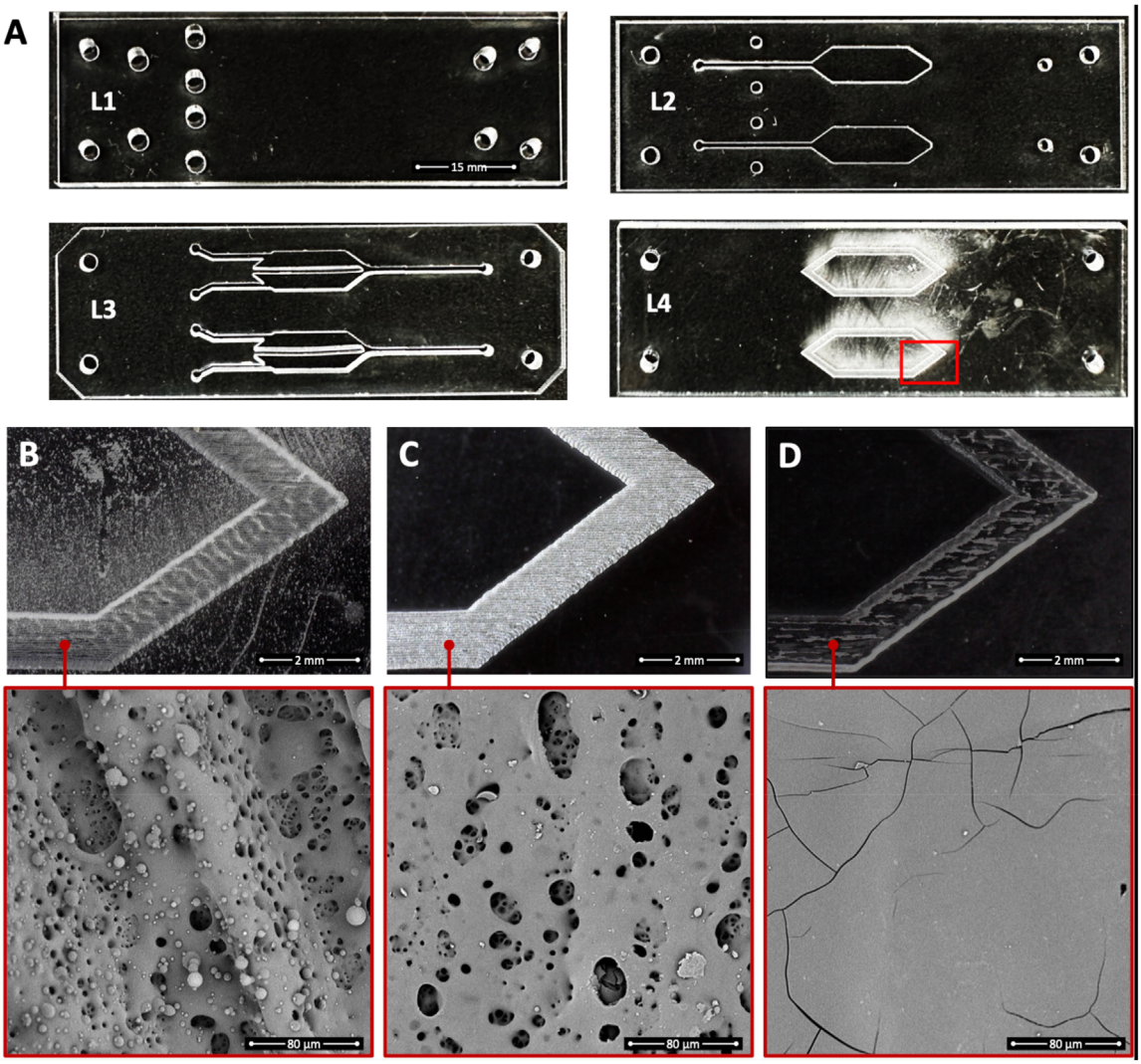

FIGURE 5 Fabrication and postprocessing of the PMMA-based microfluidic platform layers. (A) Laser-cut and engraved PMMA layers (L1–L4), showing high-fidelity reproduction of the microfluidic layout, including the structurally intact 2 mm-wide septum in layer L3 and the engraved regions in L4 designed for scaffold anchoring. (B) Optical image of the engraved area in L4 prior to cleaning, exhibiting a whitish and opaque appearance due to laser-induced debris and surface porosity. (C) Surface morphology after ultrasonic cleaning in ethanol is macroscopically unchanged, whereas SEM analysis reveals a reduction in particulates, but persistent microporosity. (D) Posttreatment with TMC vapor results in restored optical clarity and a smooth, homogeneous surface, as confirmed by SEM, with minimal residual artifacts and occasional microcracks.

dye-based tests also confirmed that fluid compartmentalization is maintained for at least 48 h, which is two times higher than the 24 h required for stable cell adhesion to the scaffold. No appreciable differences were observed between devices containing R-PLA or aligned (A-PLA) ES scaffolds. To achieve this result, several preliminary tests were carried out by varying the thicknesses of layers L2 and L3. A key challenge encountered during optimization was preventing the cell suspension droplet from touching the upper wall of the chip due to surface tension effects, which could lead to unintended contact between the two compartments. Fine-tuning the vertical spacing of the culture chamber was therefore essential to ensure stable fluid confinement and maintain strict separation between the two seeding regions.

One of the technological innovations introduced in this device is the use of an ES PLA scaffold as the cell culture substrate. PLA is a polymer widely employed in tissue engineering and is United States Food and Drug Administration approved.[38] It is also highly suitable for surface functionalization, making it adaptable for supporting different cell lines. Among the key advantages of electrospinning is the ability to control the orientation of the fibers within the scaffold.[39] This feature is particularly relevant for applications involving neural cell

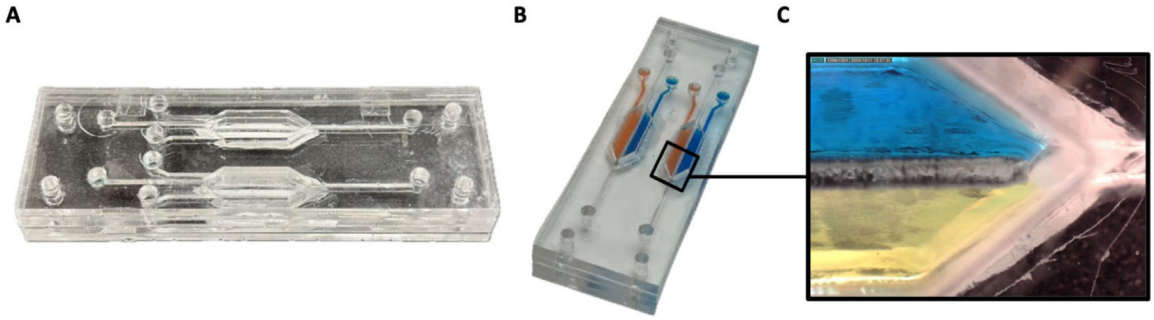

FIGURE 6 Validation of the assembly and compartmentalization performance of the microfluidic platform device. (A) Assembled chip showing precise alignment of the PMMA layers, ensured by integrated alignment pins and corner holes. (B) Simulation of the dual cell seeding process using food dyes: 80 μL of two differently colored aqueous solutions were injected into the separate compartments of the culture chamber. (C) Magnified view of the terminal region of the culture chamber, demonstrating complete surface coverage and effective fluid compartmentalization without cross-contamination. Dye separation was maintained for 48 h. No differences in compartmentalization performance were observed between devices with randomly oriented (R-PLA) or aligned (A-PLA) scaffolds.

TABLE 1 Summary of quantitative metrics describing fiber alignment, porosity, and fiber diameter of electrospun PLA scaffolds before and after their integration in the microfluidic chip.

Scaffold	Mean orientation (°)	Angular SD (°)	Alignment index	Mean porosity (%)	Mean fiber diameter (μm)
R-PLA	~0	37.0	0.05	75.4 ± 3.2	0.97 ± 0.39
A-PLA	−82.0	3.2	0.96	63.8 ± 3.8	0.90 ± 0.33
R-PLA@Chip	37.9	20.2	0.45	69.7 ± 5.8	1.07 ± 0.34
A-PLA@Chip	40.4	8.1	0.91	56.4 ± 4.3	0.97 ± 0.36

cultures. In fact, several studies have shown that the fiber orientation of ES scaffolds affects the behavior of neurons and microglial cells.[40–45]

In this study, we therefore investigated the potential of these two scaffold architectures in supporting our cell lines of interest. The evaluation was conducted under both static and dynamic conditions: static culture was used to assess biocompatibility and cell adhesion, while dynamic culture allowed us to explore the combined effects of substrate architecture and medium perfusion.

Since the scaffold assembly process involves a thermal pressing step at 70°C in the presence of ethanol for 180 s, in this study, we investigated how this treatment might affect the scaffold morphology. Figure 7A,B shows the morphology of the A-PLA and R-PLA scaffolds as fabricated while in Figure 7C,D the fiber diameter distribution and the angular distribution graphs are reported, respectively. Both A-PLA and R-PLA fibers appear regular and exhibit smooth surfaces. The fiber angular distribution reported in Figure 7D also highlight the effective fiber alignment achieved using a high-speed rotating collector. Quantitative analysis, reported in Table 1, confirmed a marked difference in fiber organization between the two scaffold types. A-PLA scaffolds exhibited a highly aligned architecture, characterized by a narrow angular dispersion and an alignment index close to unity. In contrast, R-PLA scaffolds displayed a broad angular distribution, with a large standard deviation and an alignment index close to zero, indicative of a random fiber orientation. Notably, differences in the average fiber diameters were observed: the aligned fiber membrane (A-PLA) exhibited a mean diameter of 0.90 μm, while the randomly oriented membrane (R-PLA) showed a slightly larger mean diameter of 0.97 μm. This discrepancy, although not significant, can be attributed to the mechanical tension induced by the high-speed rotation of the collector, which promotes fiber elongation and stretching of the polymer jet and is consistent with similar results in scientific literature.[46] Furthermore, from Figure 7C it is possible to observe that the fiber diameter distribution appears slightly narrower for A-PLA fibers. Another difference that emerges from this comparison is the fiber distribution and the spacing between fibers. As seen in the SEM images, the aligned fibers display smaller inter-fiber spacing compared with the R-PLA membranes, as further confirmed by porosity analysis. The A-PLA scaffolds exhibited an average porosity of 75.4 ± 3.2%, whereas the R-PLA scaffolds had a porosity of 63.8 ± 3.8%. This difference, in agreement with the morphological observations, indicates that an ordered fiber arrangement leads to reduced porosity, likely due to the denser packing associated with the aligned structure, in agreement with scientific literature.[17, 47]

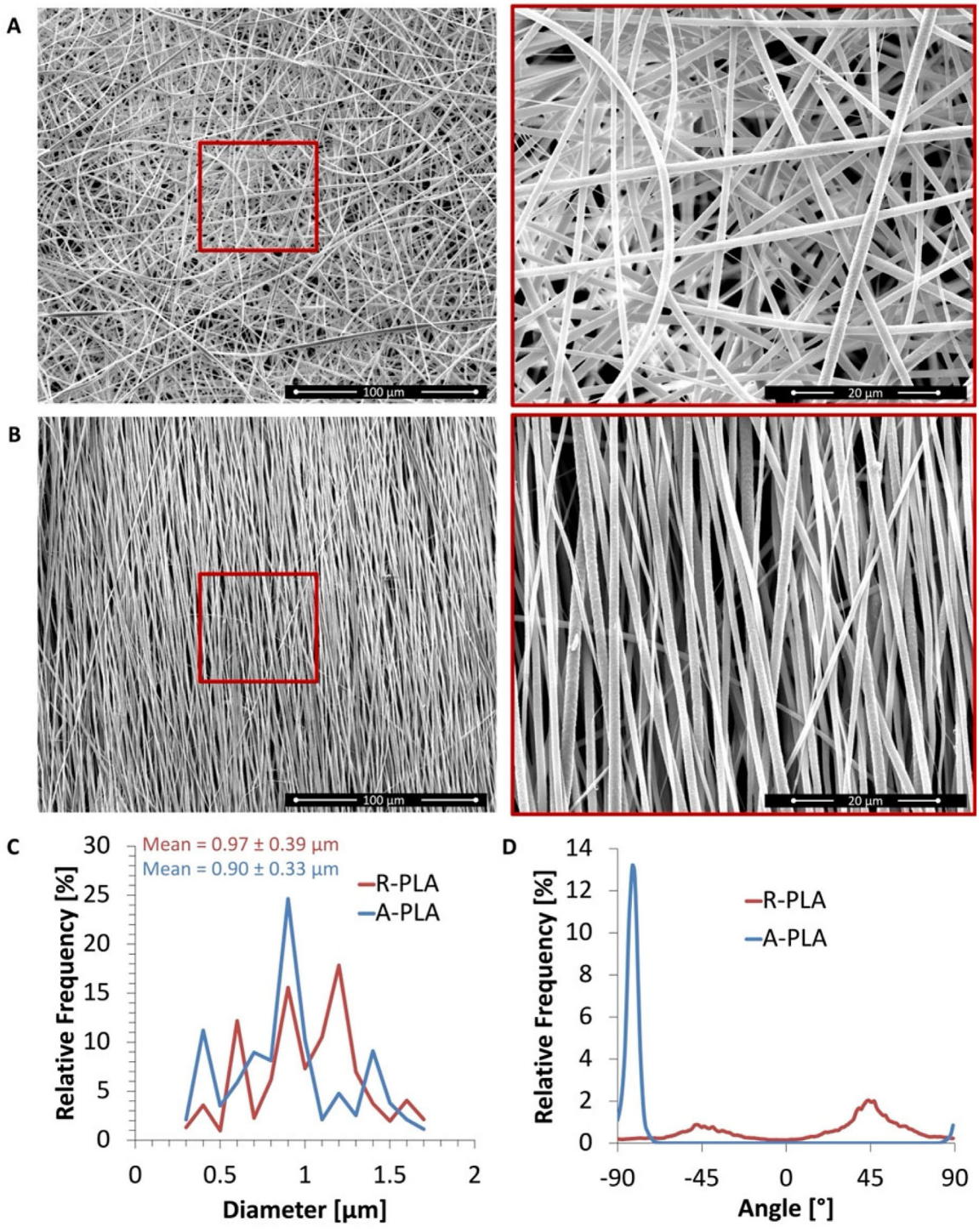

FIGURE 7 Morphological characterization of electrospun scaffolds. (A) Randomly oriented PLA (R-PLA) fibers and (B) aligned PLA (A-PLA) fibers, as observed after fabrication. (C) Fiber diameter distribution and (D) angular distribution of A-PLA and R-PLA scaffolds.

To assess whether the integration process preserves the structural integrity and functional role of the ES scaffolds within the chip, further morphological analyses were performed. As schematically illustrated in Figure 8A, the morphology of the ES scaffolds integrated and then extracted from the chips was evaluated in the area surrounding the septum that separates the two compartments and, at higher magnification, in a region located approximately 500 µm from it. As expected, the portion of the scaffold positioned directly beneath the septum appeared severely damaged, confirming that the septum effectively provides physical separation between the two culture regions. In fact, the loss of porous structure beneath the septum prevents fluid crossover between compartments driven by

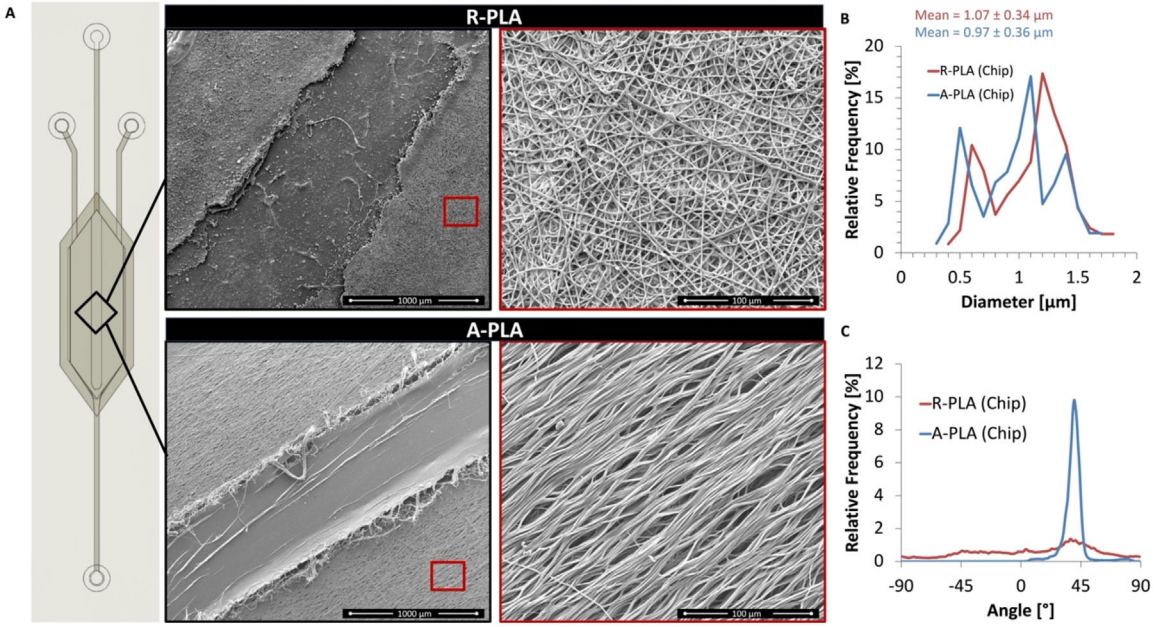

FIGURE 8 SEM analysis of scaffold morphology near the septum within the assembled microfluidic platform device. (A) The left image schematically illustrates the visualized region beneath the septum. The right images are approximately 500 µm away from the septum. (B) Fiber diameter distribution and (C) angular distribution of A-PLA and R-PLA scaffolds extracted from the microfluidic device after assembly.

capillary forces. In contrast, the area adjacent to the septum displayed regular fibers that were not affected by the presence of the dividing structure.

Notably, after the assembly process, the fibers appeared slightly fused together, likely due to localized thermal or mechanical effects during bonding. However, this did not significantly affect the average fiber diameter that increase of about 10% for both A-PLA and R-PLA scaffolds probably due to a swelling phenomenon induced by the presence of ethanol traces during the thermal bonding. Overall, the fiber distribution behavior remained comparable to pristine one (Figure 8B). In aligned scaffolds, the fibers also exhibited a slightly more undulated morphology compared with their preassembled state, although the degree of alignment remained quite high, as depicted in Figure 8C. It remains unclear whether this waviness results from the chip fabrication process itself or from the disassembly procedure required to expose the scaffold for SEM observation. As reported in Table 1, the porosity of the scaffolds extracted from the chip was found to be about 6–7% lower than the as-fabricated systems. More in detail, the R-PLA scaffold porosity was about 70% while for A-PLA the porosity was about 56%. This reduction in porosity can be attributed to fiber thickening induced by polymer swelling, together with a denser fiber packing resulting from the scaffold inclusion within the chip at 70°C for 180 s in presence of ethanol. While native brain tissue exhibits lower porosity values (0.18–0.30),[48] this parameter refers to the extracellular space at the cellular scale. In contrast, the higher porosity of the ES scaffolds developed in this work (56–70%) reflects the void fraction of a fibrous network designed to support cell adhesion and proliferation, in agreement with literature on ES substrates.[49–51]

R-PLA scaffolds integrated within the chip largely preserved their random fibrous architecture. Although minor angular biases were observed, the broad angular dispersion and low alignment index indicate the absence of a strong preferential orientation, confirming that chip integration does not substantially alter the intrinsic isotropic organization of R-PLA scaffolds (Table 1). On the other hand, A-PLA scaffolds integrated within the chip exhibited a pronounced preferential fiber orientation, characterized by a narrow angular dispersion and a high alignment index. Although the degree of alignment was slightly reduced compared with bulk A-PLA scaffolds, the architecture remained strongly anisotropic.

Morphological analysis revealed that fiber organization was primarily driven by electrospinning conditions and largely preserved after integration within the chip. A-PLA scaffolds retained a strongly anisotropic architecture, with only a slight relaxation of alignment likely induced by device assembly. In contrast, R-PLA scaffolds remained predominantly isotropic both in bulk and after chip integration, with no evidence of a meaningful global preferential orientation. Overall, chip integration did not override the intrinsic scaffold microarchitecture, enabling a controlled comparison of anisotropic and isotropic substrates within the same microfluidic platform.

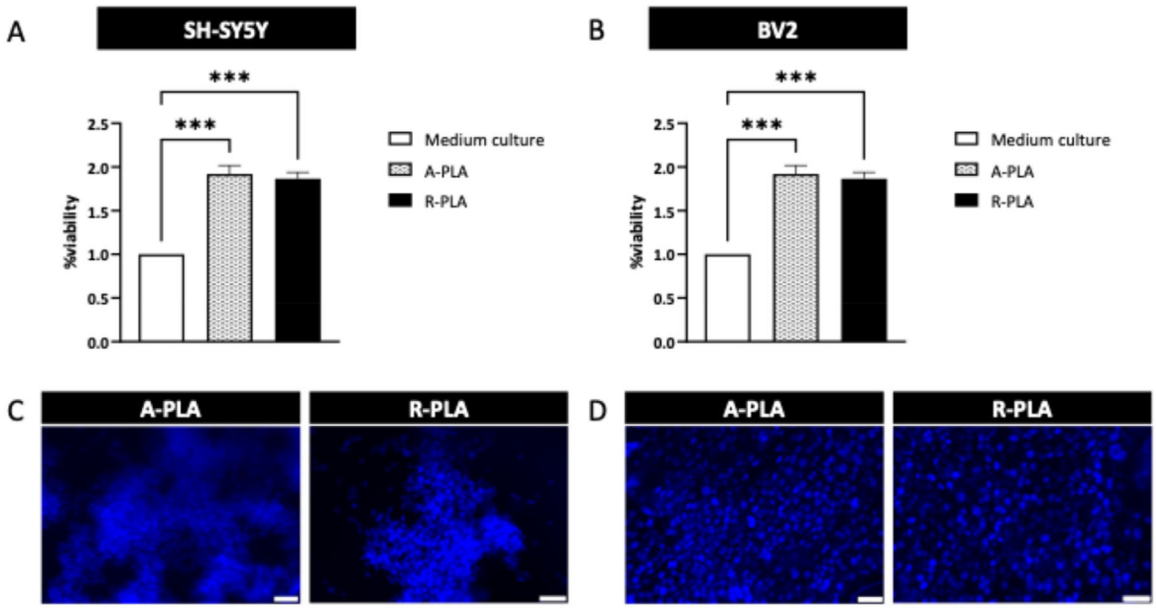

FIGURE 9 Cytocompatibility assessment of A-PLA and R-PLA fibers on BV2 and SH-SY5Y cells. (A and B) Cell viability was evaluated by MTS assay on SH-SY5Y (A) and BV2 (B) cell lines seeded on A-PLA and R-PLA fibers. Formazan production was measured by optical density (O.D.) at 490 nm after 24 h. O.D. values were normalized to the culture medium values to assess the cytocompatibility. (C and D) Representative fluorescence microscopy images of SH-SY5Y (C) and BV2 (D) cells stained with Hoechst to visualize nuclei after 24 h of culture on the fibers. Data are presented as mean ± SEM of three independent experiments. Statistical analysis was performed by two-way ANOVA followed by Dunnett's multiple comparisons test, ***$p \leq .001$. Scale bar: 50 μm.

3.3 | Cytocompatibility and cell attachment

In the CNS, neurons and microglia have been tested for this system because they are among the most studied cells in in vitro models for pharmacological treatment, especially in the context of neurodegenerative and neuroinflammatory diseases, for a variety of reasons. Neurons, in particular, are the primary cells of the CNS, characterized by their electrical activity, and are the direct target of numerous diseases (Alzheimer's, Parkinson's, ALS, epilepsy, stroke, etc.).[52] In contrast, microglia, the brain's resident immune cells, act as sentinel cells, regulating the inflammatory response. These cells have been observed to be activated in a wide range of neurological diseases, resulting in the release of cytokines, free radicals, and neurotoxic or neuroprotective factors.[53] The cytocompatibility of A-PLA and R-PLA fibers was assessed on the BV2 and SH-SY5Y cell lines using the MTS assay. The results of the MTS assay, shown in Figure 9A,B, were analyzed by evaluating the formazan concentration measured in optical density (O.D.) at 490 nm. To verify the cytocompatibility, the test was performed 24 h after seeding. The primary purpose of this analysis was to evaluate whether the cells plated on the ES membrane were not only able to adhere but also to be viable. The data show that the cells have adhered to the fibers and are metabolically active, as demonstrated by the ability to reduce MTS to formazan, an indicator of cell viability. The presence of cells on the fibers and their ability to support cell adhesion and growth were also confirmed by staining the nuclei with Hoechst (Figure 9C,D).

To investigate how scaffold fiber orientation influences early cell attachment and their spatial organization, SEM images of BV2 and SH-SY5Y cells cultured for 24 h on both A-PLA (Figure 10A) and R-PLA (Figure 10B) scaffolds were acquired. SEM imaging performed after 24 h of static culture confirmed good cell adhesion on both aligned (A-PLA) and random (R-PLA) ES scaffolds. On both substrates, cells appeared well spread on the fibrous matrix and formed interconnected clusters, indicating the establishment of early cell–cell contacts. Moreover, a qualitative directional organization could already be observed on A-PLA scaffolds, where cellular bodies tended to elongate following the predominant fiber direction, while on R-PLA no preferential orientation was visually detected. These qualitative observations were further validated through angular distribution analysis (Figure 10C) to precisely quantify the influence of scaffold topology on cell orientation. BV2 cultured on A-PLA showed the highest degree of orientation (peak frequency: 9%), indicating a clear alignment along the fiber axis, whereas the same cells on random fibers (R-PLA) exhibited a nearly uniform angular distribution (0.7%). A similar trend was observed for SH-SY5Y cells, with a pronounced preferential

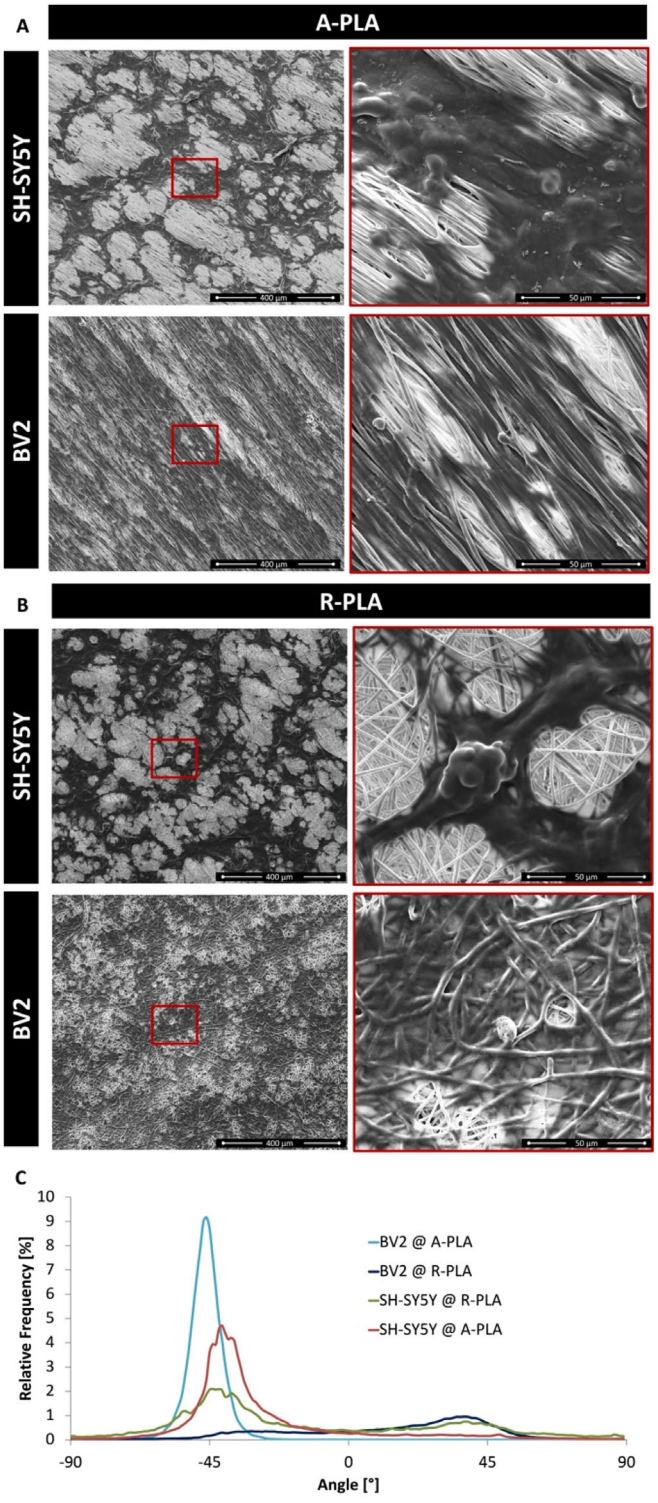

FIGURE 10 SEM images of SH-SY5Y and BV2 cells cultured on (A) aligned (A-PLA) and (B) random (R-PLA) electrospun scaffolds for 24 h. (C) Angular distribution analysis of SH-SY5Y and BV2 cells cultured for 24 h on A-PLA and R-PLA scaffolds.

directionality on A-PLA (4.2%) compared with a minimal alignment on R-PLA (1.2%). These results confirm that aligned topographical cues effectively guide CNS-relevant cell orientation, while random architectures do not provide preferential guidance. The marked topographical response, particularly evident in BV2 cells, demonstrates that the architecture of ES fibers directly influences cellular spatial behavior, reinforcing the suitability of this platform for modeling CNS-like structural anisotropy. This phenomenon could be ascribed to the alignment of microfibers, which function as a physical guide for the cell extensions, thereby influencing both their direction of growth and overall morphology. Indeed, it has been demonstrated that substrates exhibiting oriented patterns promote the alignment and elongation of neurites, thereby facilitating the formation of coherent connections between neuronal cells and, in general, a physiological-like environment for drug testing.[45]

3.4 | Evaluation of cellular structural markers

Beta-tubulins represent one of two structural components that constitute the microtubule network. While general tubulins have been demonstrated to play a role in a wide range of cellular processes (mitosis, motility, etc.), the specific localization of beta-tubulin III in neurons has been determined. In particular, the expression of beta-tubulin III is pivotal to axon maintenance. Following the discovery that the human brain generates new neurons from pools of stem cells, beta-tubulin III has been utilized as a marker of positive neuronal identity in numerous research studies.[54, 55] The present study analyzed the presence of these markers as an indicator of the structural and functional status of the neuronal and axonal cytoskeleton. Immunofluorescent analysis revealed high levels of fluorescence in SH-SY5Y neuronal cells plated on random and aligned membranes, indicating significant β-tubulin III expression (Figure 11A). This suggests that the presence of the two membrane types does not alter the correct and functional structure of the microtubule cytoskeleton.

Furthermore, in order to assess whether the arrangement of fibers influences the structural organization of neuronal projections, a quantitative analysis was conducted of the angular distribution of axons highlighted by βIII-tubulin staining on both types of membrane (Figure 11B).

In the presence of the aligned fiber membrane, the axonal extensions show a clear tendency to arrange themselves along the main axis of the fibers, while this

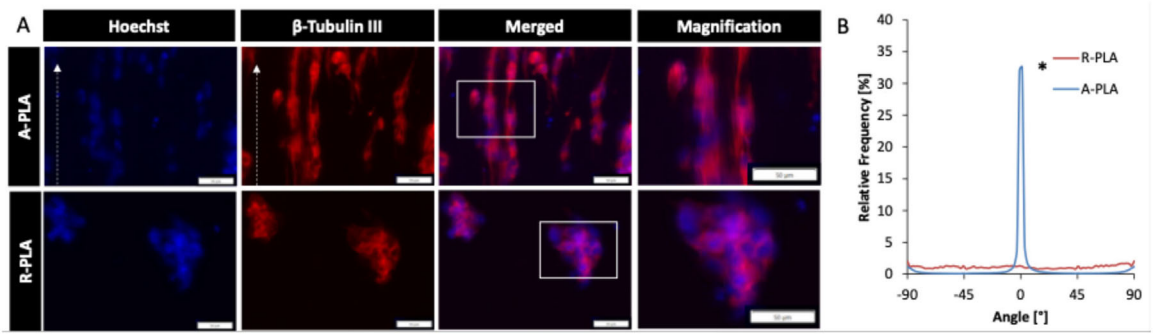

FIGURE 11 Immunofluorescent distribution of β-tubulin III and MAP2 in SH-SY5Y cells cultured on random and aligned fiber membranes. (A) Representative images of Immunostaining for β-tubulin III (red), Hoechst (blue). The white arrows indicate the direction of the aligned fibers. Bar: 50 μm. (B) Quantitative analysis of the angular distribution of neurites, obtained using the ImageJ directionality tool. The graph shows the distribution of orientation angles (from −90° to +90°) of βIII-tubulin-positive projections. It highlights that, compared with a wider and more isotropic distribution observed in randomly oriented fiber membranes, there is a narrow distribution centered around 0° in the case of aligned membranes. All data presented are the mean ± SEM of at least three independent experiments; Statistical analysis was performed by comparing aligned and random membrane replicates at each orientation angle using an unpaired, two-tailed Student's *t*-test. $*p < .05$.

preferential orientation is not observable in the case of the randomly oriented fiber membrane, in which the neuronal projections are distributed isotropically. The angular distribution profiles confirm a narrow distribution centered around 0° for the aligned membrane, compared with a wider and more uniform distribution in the case of the random membrane, indicating a different degree of spatial organization of neuronal projections depending on the architecture of the scaffold.

IBA1 is a widely utilized marker for the identification of microglia and macrophages, due to its specific expression in these cell populations. The IBA1 protein, a 17-kDa cytoplasmic protein belonging to the S100 superfamily, is encoded by the AIF1 (allograft inflammatory factor 1) gene. The protein is characterized by the presence of two EF-hand domains, which facilitate calcium binding, thus enabling interaction with components of the actin cytoskeleton. These interactions modulate key processes such as cell morphology, migration, and phagocytosis. In contrast to other calcium-binding proteins, the primary function of which is to regulate intracellular signaling, IBA1 plays a direct role in the process of actin aggregation. This, in turn, contributes to the dynamics of the cytoskeleton and the morphofunctional plasticity of immune cells.[56, 57] The present study analyzed the presence of this marker as an indicator of the structural and functional status of the BV2 in presence of A-PLA and R-PLA fibers. Immunofluorescent analysis revealed that all BV2 microglial cells exhibit high levels of fluorescence in both random and aligned membranes, indicating significant IBA1 expression (Figure 12A). This suggests that the presence of the two membrane types does not alter the well-structured and organized cytoskeleton of cells.

Furthermore, quantitative analysis of fluorescence intensity (Figure 14B) did not reveal any statistically significant differences between cells cultured on aligned membranes and those on randomized membranes, indicating that fiber architecture does not induce variations in IBA1 expression for a specific type of membrane.

3.5 | Chip for assessing cell-specific drug selectivity

In recent years, significant number of nanostructured carriers were designed to deliver drugs to specific sites or cells with high efficiency.[58] Functional nanocarriers such as liposomes, dendrimers, nanovesicles, and nanoparticles, along with hydrogels and bioresponsive polymers, have enabled precise, efficient, and targeted delivery of therapeutics, improving drug stability, bioavailability, and site-specific release.[20, 21, 59–68] The objective of the present study was to verify the effectiveness of the microfluidic platform in assessing the selectivity of the drugs or a drug delivery system toward a specific cell type when a drug or vector is perfused under physiological interstitial velocities. In order to achieve this objective, a targeted delivery system that had been well-validated and had been in existence for a considerable time was utilized. This brain drug delivery system consists of nanovesicles derived from myelin extracted from brain tissue, known as MyVes, which have been demonstrated to exhibit a high affinity for microglial cells.[20, 21]

The MyVes, conjugated to a fluorophore (MyVes-Atto633), were introduced into the chip via continuous flow and incubated for a period of 2 h. The

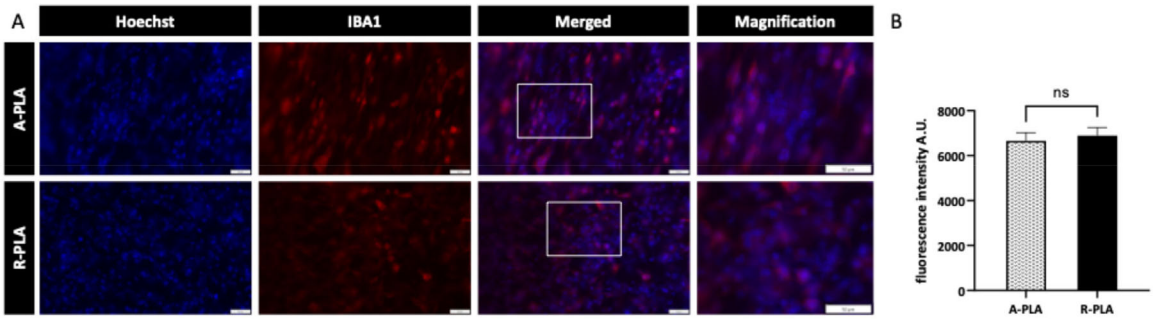

FIGURE 12 Immunofluorescent distribution of IBA1 in BV2 cells cultured on random and aligned fiber membranes. (A) Representative images of Immunostaining for IBA1 (red), Hoechst (blue). Scale bar: 50 μm. (B) Quantitative analysis of IBA1 fluorescence intensity in cells cultured on aligned and randomly oriented fiber membranes. All data are presented as mean ± SEM of at least three independent experiments. Statistical analysis was performed using an unpaired Student's *t*-test. ns = not significant.

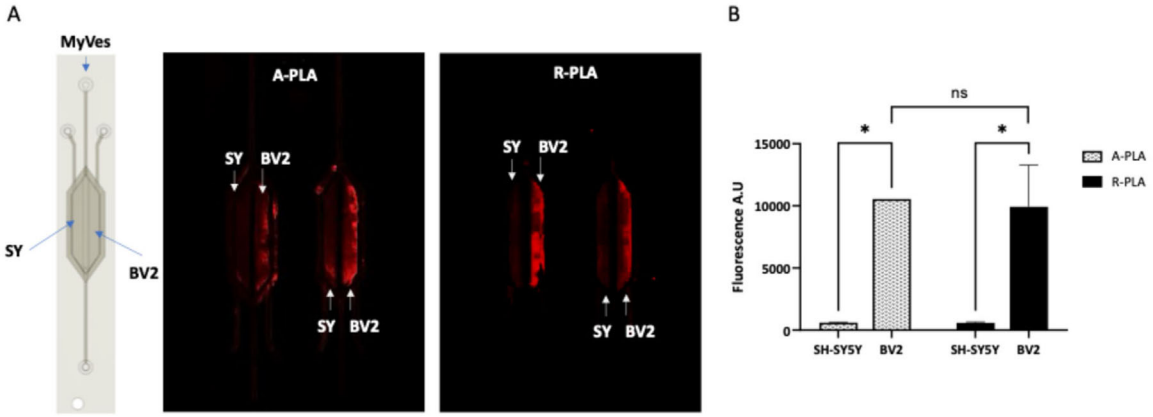

FIGURE 13 Fluorescence analysis of MyVes-Atto633 interaction with microglial and neuronal cells cultured in microfluidic chips. Fluorescently labeled MyVes were introduced into the microfluidic chip and incubated under continuous flow for 2 h. (A) The fluorescence images of the chips were detected using fluorescence laser scanner Typhoon FLA 9000. (B) Representative histogram of the quantitative analysis of the red fluorescence intensity of labeled MyVes, assessed in chambers containing SH-SY5Y and BV2 cells grown on aligned and randomly oriented fiber membranes. Fluorescence intensity was quantified after background subtraction and normalization for the selected area. Data are expressed as the mean ± SEM of at least three independent experiments. Statistical analysis was performed by two-way ANOVA followed by Šídák's multiple comparisons test, ns = not significant, $*p \leq .05$.

interaction between the vesicles and the cells was subsequently analyzed by fluorescence imaging, using both a fluorescence scanner, which allows for the analysis of the entire chip surface and the simultaneous visualization of the two chambers containing the different cell lines, and high-resolution fluorescence microscopy, for a detailed characterization of vesicle–cell interactions. Fluorescence scanning analysis (Figure 13A,B) revealed marked fluorescence exclusively in chambers containing microglial cells, both in the A-PLA and R-PLA chips. This outcome validates the elevated selectivity of MyVes for the microglial population and substantiates that the chip-based system facilitates the discernment of the interaction of molecules, drugs, or drug delivery systems with particular cell types that coexist within the same microenvironment.

The chip was then subjected to analysis by means of fluorescence microscopy (Figure 14A,B). The use of 4X magnification facilitated the concurrent visualization of both chambers, which were separated by the central septum. Fluorescence was found to be localized exclusively in the compartment containing microglial cells, thus confirming the data obtained by the fluorescence scanner. This result strengthens the evidence of MyVes selectivity for the microglial population and underscores the validity of the chip as an experimental platform for studying the selectivity of drugs or delivery systems toward specific cell types in a controlled dynamic microenvironment.

The results obtained show that the chip developed represents a significant advance over currently available models. The integration of an ES membrane within a microfluidic

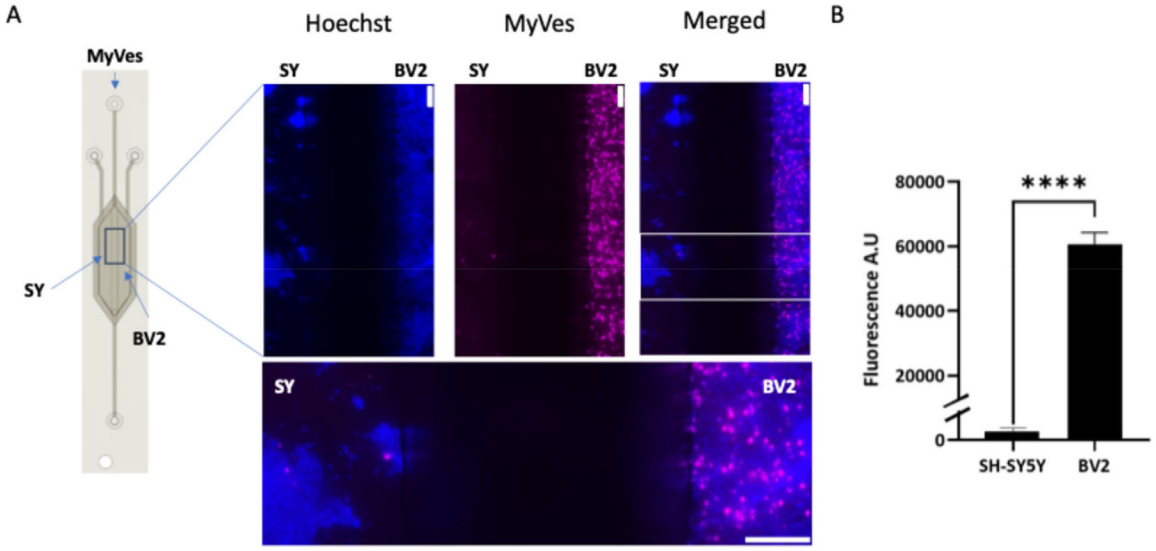

FIGURE 14 Fluorescence microscopy analysis of MyVes-Atto633 distribution in the microfluidic chip. (A) Representative image of MyVes labeled with Atto 633 (purple) and Nuclei with Hoechst (blue) were acquired at 4× magnification. (B) Representative histogram of the quantitative analysis of the fluorescence intensity of labeled MyVes, assessed in chambers containing SH-SY5Y and BV2 cells grown on aligned and randomly oriented fiber membranes. Data are expressed as the mean ± SEM of at least three independent experiments. Statistical analysis was performed by Student's *t*-test, $p \leq .0001$.

platform is a highly innovative feature, as it combines the structural biomimetics typical of fibrous materials with the spatial and dynamic control characteristic of OoC systems. Added to this is the possibility of cocultivating two distinct cell populations in separate compartments but immersed in the same fluid environment, allowing the study of drug selectivity in conditions that partially reproduce physiology, such as cell communication. Furthermore, the use of thermoplastic materials and rapid prototyping techniques overcomes the scalability limitations of PDMS devices, while fluid dynamics simulations confirm the system's ability to maintain flow rates compatible with those found in the interstitial space of the brain. Overall, the platform is a simplified but functional CNS model, capable of sustaining cell viability under flow conditions and providing reliable readings on the selectivity of therapeutic compounds. Despite significant technological advances, the system has some limitations. The use of only two cell lines reduces the biological complexity of the model, and the absence of the blood–brain barrier (BBB) limits the ability to predict the actual bioavailability of drugs in the CNS. Furthermore, the lack of a systemic inflammatory component prevents exploration of how pathological conditions can modulate drug selectivity.

These aspects outline clear directions for development. In fact, the system could be integrated with a module that reproduces the BBB, representing an evolutionary step to increase the physiological relevance of the system, as well as the introduction of controlled inflammatory components to model pathological states. Furthermore, we do not rule out the possibility of expanding the number of compartments and cell types.

Finally, the integration of in-line sensors and adaptation to high-throughput automatable formats could promote the adoption of the device as a versatile tool for preclinical screening.

Overall, the proposed platform represents a significant contribution toward more predictive and physiologically relevant in vitro models for the study of drug selectivity in the CNS.

4 | Conclusion

This work presented the design, fabrication, and validation of an innovative microfluidic platform specifically engineered to investigate drug selectivity within heterogeneous neural cells. The device integrates an ES PLA-based scaffold within an innovative microfluidic architecture, allowing the coculture of distinct cell populations in spatially separated compartments that communicate through a shared perfusion environment. By modulating flow parameters to reproduce physiological or pathological fluid velocities, the system enables in vivo like drug delivery and the assessment of compound selectivity. A key feature of the platform lies in the fluidic isolation during cell seeding and subsequent interaction during perfusion, without compromising scaffold integrity or cell adhesion. The results obtained demonstrate that brain cells adhere effectively to both aligned and random fibers,

showing a preferential orientation on A-PLA scaffolds. Moreover, analysis of structural proteins confirmed that both types of substrates are able to maintain physiological cellular organization, suggesting their suitability as substrate for advanced brain tissue models. As a proof of concept, the microfluidic chip was tested by coculturing the two cell populations, neurons and microglia, and to assess the selective response to myelin-derived nanovesicles under physiological flow conditions, compatible with those found in the interstitial space of the brain. The MyVes selectivity on microglial cells was demonstrated when perfused in the microfluidic platform simulating a controlled physiological environment in terms of fluid velocity over the cells. The data obtained lend support to the validity of the proposed system as a versatile platform for advanced studies of drug selectivity and drug screening. Future developments will focus on the integration of hybrid scaffold materials composed of both natural and synthetic materials, increased cellular complexity, and integration of vascular and sensing modules to further enhance physiological relevance and readout.

AUTHOR CONTRIBUTIONS

Conceptualization: Francesco Lopresti, Maria Testa, Pasquale Picone, and Laura Palumbo. *Formal analysis*: Maria Testa, Martina La Rosa, and Laura Palumbo. *Funding acquisition*: Francesco Lopresti, Vincenzo La Carrubba, Pasquale Picone, and Domenico Nuzzo. *Investigation*: Maria Testa, Martina La Rosa, Fabio Salvatore Palumbo, Laura Palumbo, and Antonella Girgenti. *Methodology*: Francesco Lopresti, Vincenzo La Carrubba, Pasquale Picone, and Domenico Nuzzo. *Resources*: Francesco Lopresti, Vincenzo La Carrubba, Fabio Salvatore Palumbo, Pasquale Picone, and Domenico Nuzzo. *Supervision*: Francesco Lopresti, Vincenzo La Carrubba, Pasquale Picone, and Domenico Nuzzo. *Writing—original draft*: Maria Testa, Francesco Lopresti, Pasquale Picone, and Laura Palumbo. *Writing—review and editing*; Maria Testa, Martina La Rosa, Francesco Lopresti, Pasquale Picone, Domenico Nuzzo, Laura Palumbo, and Antonella Girgenti.

ACKNOWLEDGMENTS

The authors acknowledge Mr. Salvatore Tornabene for the support in the microfluidic platform fabrication.

Open access publishing facilitated by Universita degli Studi di Palermo, as part of the Wiley - CRUI-CARE agreement.

FUNDING

This research was partially supported by EU funding within the MUR PNRR "National Center for Gene Therapy and Drugs based on RNA Technology" (Project no. CN00000041 CN3 RNA); the PNRR project "Ecosistema dell'Innovazione Sicilian MicronanoTech Research And Innovation Center (SAMOTHRACE, ECS00000022)", Spoke 3 – WP 5 – T5.2.1; the National Recovery and Resilience Plan (NRRP), Mission 4, Component 2, Investment 1.1, Call for tender No. 104 published on 2.2.2022 by the Italian Ministry of University and Research (MUR), funded by the European Union – NextGenerationEU – Project Title Green MIcrofluiDic PLAtform for advanced tissue on a Chip culturEs (Green MID-PLACE) – CUP: B53D23005870006 Grant Assignment Decree No. 961 adopted on 30/06/2023 by the Italian Ministry of Ministry of University and Research (MUR); and the European Union - Next Generation EU - NRRP M6C2 - Investment 2.1 Enhancement and strengthening of biomedical research in the NHS.

CONFLICT OF INTEREST STATEMENT

The authors declare no conflict of interest.

DATA AVAILABILITY STATEMENT

The data presented in this study are available on request from the corresponding author.

ORCID

Francesco Lopresti https://orcid.org/0000-0003-3893-0820

REFERENCES

1. T. Wang, O. I. Pulkkinen, T. Aittokallio, *Front. Pharmacol.* **2022**, *13*, 1003480.
2. M. T. Manzari, Y. Shamay, H. Kiguchi, N. Rosen, M. Scaltriti, D. A. Heller, *Nat. Rev. Mater.* **2021**, *6*, 351.
3. Z. Zhao, A. Ukidve, J. Kim, S. Mitragotri, *Cell* **2020**, *181*, 151.
4. A. Żuchowska, P. Baranowska, M. Flont, Z. Brzózka, E. Jastrzębska, *Anal. Chim. Acta* **2024**, *1301*, 342413.
5. R. Xie, V. Pal, Y. Yu, X. Lu, M. Gao, S. Liang, M. Huang, W. Peng, I. T. Ozbolat, *Biomaterials* **2024**, *304*, 122408.
6. G. Pagnotta, S. Kalia, L. Di Lisa, A. F. G. Cicero, C. Borghi, M. L. Focarete, *Bioprinting* **2022**, *27*, e00218.
7. Y. Zhao, S. Landau, S. Okhovatian, C. Liu, R. X. Z. Lu, B. F. L. Lai, Q. Wu, J. Kieda, K. Cheung, S. Rajasekar, K. Jozani, B. Zhang, M. Radisic,, *Nat. Rev. Bioeng.* **2024**, *2*, 588.
8. S. Nath, G. R. Devi, *Pharmacol. Ther.* **2016**, *163*, 94.
9. D. L. Puhl, J. L. Funnell, D. W. Nelson, M. K. Gottipati, R. J. Gilbert, *Bioeng.* **2021**, *8*, 1.
10. W. Du, T. Wang, S. Hu, J. Luan, F. Tian, G. Ma, J. Xue, *Engineered Regeneration* **2023**, *4*, 289.
11. H. B. Wang, M. E. Mullins, J. M. Cregg, C. W. McCarthy, R. J. Gilbert, *Acta Biomater.* **2010**, *6*, 2970.
12. I. A. Hammam, R. Winters, Z. Hong, *Biomed. Eng. Adv.* **2024**, *8*, 100132.
13. Y. You, C. Zhang, Z. Guo, F. Xu, D. Sun, J. Xia, S. Chen, *Microfluid Nanofluidics* **2024**, *28*, 45.
14. R. S. Fardous, S. Alshmmari, E. Tawfik, I. Khadra, Q. Ramadan, M. Zourob, *ACS Appl. Mater. Interfaces* **2024**, *16*, 40767.

15. Z. Wang, S. Liu, M. Han, J. Xu, M. Qin, Q. Yang, G. Zeng, M. Long, T. Li, J. Yin, L. Yu, W. Huang, L. Wang, Y. Wu,, *Adv. Fiber Mater.* **2024**, *6*, 1521.
16. M. Testa, M. Loria, F. Lopresti, C. Di Marco, M. Kersaudy-Kerhoas, F. Bucchieri, M. Pucci, E. Costanzo, S. Scilabra, R. Alessandro, *Lab Chip* **2025**.
17. E. Capuana, M. Testa, C. D. Marco, F. Lopresti, V. La Carrubba, *Adv Healthc Mater* **2025**, *14*(25), 2500378.
18. Y. Liu, L. Sun, H. Zhang, L. Shang, Y. Zhao, *Chem. Rev.* **2021**, *121*, 7468.
19. A. Liga, J. A. S. Morton, M. Kersaudy-Kerhoas, *Microfluid Nanofluidics* **2016**, *20*, 164.
20. P. Picone, F. S. Palumbo, F. Cancilla, A. Girgenti, P. Cancemi, V. Muccilli, A. D. Francesco, M. Cimino, C. Cipollina, M. Soligo, L. Manni, G. Sferrazza, L. Scalisi, D. Nuzzo,, *Acta Biomater.* **2024**, *187*, 352.
21. P. Picone, F. S. Palumbo, S. Federico, G. Pitarresi, G. Adamo, A. Bongiovanni, A. Chaves, P. Cancemi, V. Muccilli, V. Giglio, V. Vetri, S. Anselmo, G. Sancataldo, V. Di Liberto, D. Nuzzo, *Mater. Today Bio.* **2021** *12*, 100146.
22. F. Lopresti, F. Carfì Pavia, I. Vitrano, M. Kersaudy-Kerhoas, V. Brucato, V. La Carrubba, *J. Mech. Behav. Biomed. Mater.* **2020**, *101*, 103449.
23. M. Testa, M. Gaggianesi, C. D'Accardo, G. Porcelli, A. Turdo, C. Di Marco, B. Patella, S. Di Franco, C. Modica, S. Di Bella, F. Lopresti, G. Stassi, V. La Carrubba, M. Todaro, *Int. J. Mol. Sci.* **2025**, *26*, 1028.
24. T. L. Place, F. E. Domann, A. J. Case, *Free Radic Biol Med* **2017**, *113*, 311.
25. Z. Liu, G. Song, C. Zou, G. Liu, W. Wu, T. Yuan, X. Liu, *Free Radic Biol Med* **2015**, *84*, 42.
26. Z. Xun, D. Lee, J. Lim, C. A. Canaria, A. Barnebey, S. M. Yanonne, C. T. McMurray, *Mech. Ageing Dev.* **2012**, *133*, 176.
27. F. Lopresti, S. Campora, S. Rigogliuso, A. Nicosia, A. Lo Cicero, C. Di Marco, S. Tornabene, G. Ghersi, V. La Carrubba, *Int. J. Mol. Sci.* **2024**, *25*, 2507.
28. F. Lopresti, S. Campora, G. Tirri, E. Capuana, F. Carfì Pavia, V. Brucato, G. Ghersi, V. La Carrubba, *Materials Science and Engineering: C* **2021**, *127*, 112248.
29. N. A. Hotaling, K. Bharti, H. Kriel, C. G. Simon, *Biomaterials* **2015**, *61*, 327.
30. A. Bernasconi, F. Cosmi, P. J. Hine, *Compos. Sci. Technol.* **2012**, *72*, 2002.
31. A. Zilberman, R. C. Cornelison, *Brain Res. Bull.* **2021**, *174*, 72.
32. G. S. Ugolini, D. Cruz-Moreira, R. Visone, A. Redaelli, M. Rasponi, *Micromachines* **2016**, *7*, 233.
33. X. Wan, S. Ball, F. Willenbrock, S. Yeh, N. Vlahov, D. Koennig, M. Green, G. Brown, S. Jeyaretna, Z. Li, Z. Cui, H. Ye, E. O'Neill, *Sci. Rep.* **2017**, *7*, 9408.
34. H. Moghadas, M. S. Saidi, N. Kashaninejad, N. Nguyen, *Drug Deliv Transl Res* **2018**, *8*, 830.
35. P. M. Keeney, L. D. Dunham, C. K. Quigley, S. L. Morton, K. E. Bergquist, J. P. Bennett, *Exp. Neurol.* **2009**, *220*, 374.
36. M. Cloutier, F. B. Bolger, J. P. Lowry, P. Wellstead, *J. Comput. Neurosci.* **2009**, *27*, 391.
37. I. R. G. Ogilvie, V. J. Sieben, C. F. A. Floquet, R. Zmijan, M. C. Mowlem, H. Morgan, *J. Micromech. Microeng.* **2010**, *20*, 065016.
38. J. E. Ogbu, C. I. Idumah, *Int. J. Polymeric Mater. Polymeric Biomater.* **2025**, *74*, 497.
39. M. Oroujzadeh, E. Mosaffa, S. Mehdipour-Ataei, *Surfaces and Interfaces* **2024**, 104386.
40. M. Licciardello, C. Traldi, M. Bortolameazzi, D. Testore, G. Ciardelli, C. Tonda-Turo, *Front. Biomater. Sci.* **2024**, *3*, 1362599.
41. S. Lee, M. Nowicki, B. Harris, L. G. Zhang, *Tissue Eng. Part A* **2017**, *23*, 491.
42. A. Subramanian, U. M. Krishnan, S. Sethuraman, *Biomed. Mater.* **2011**, *6*, 025004.
43. K. Nutt, Z. Dombros-Ryan, R. Birea, E. V. Franks, S. Eastham, M. Godwin, C. F. Adams, D. M. Chari, S. I. Jenkins, *Micromachines* **2025**, *16*, 256.
44. D. L. Puhl, J. L. Funnell, D. W. Nelson, M. K. Gottipati, R. J. Gilbert, *Bioeng.* **2020**, *8*, 4.
45. F. Yang, R. Murugan, S. Wang, S. Ramakrishna, *Biomaterials* **2005**, *26*, 2603.
46. A. M. El-hadi, F. Y. Al-Jabri, *Polymers* **2016**, *8*, 97.
47. U. Stachewicz, P. K. Szewczyk, A. Kruk, A. H. Barber, A. Czyrska-Filemonowicz, *Materials Science and Engineering: C* **2019**, *95*, 397.
48. T. Yuan, L. Shen, D. Dini, *Acta Biomater.* **2024**, *173*, 123.
49. L. Ruccolo, A. Evangelista, M. Benazzo, B. Conti, S. Pisani, *Int. J. Mol. Sci.* **2025**, *26*, 9528.
50. Y. Gao, Z. Tang, Z. Wu, J. Zhang, J. Ma, S. Liu, Y. Wang, *Biomater Sci* **2025**, *13*, 5278.
51. Y. Li, Y. Zhang, Y. Fu, Y. Lu, K. Jiang, L. Li, Q. Liu, A. Dupuy, L. A. Ju, Y. Wang, *Rare Met.* **2025**, *44*(7), 4315.
52. D. G. Gadhave, V. V Sugandhi, S. K. Jha, S. N. Nangare, G. Gupta, S. K. Singh, K. Dua, H. Cho, P. M. Hansbro, K. R. Paudel, *Ageing Res. Rev.* **2024**, *99*, 102357.
53. L. Palumbo, M. Carinci, A. Guarino, L. Asth, S. Zucchini, S. Missiroli, A. Rimessi, P. Pinton, C. Giorgi, *Biomedicines* **2023**, *11*, 2825.
54. C. D. Katsetos, A. Legido, E. Perentes, S. J. Mörk, *J. Child Neurol.* **2003**, *18*, 851.
55. P. Binarová, J. Tuszynski, *Cells* **2019**, *8*, 1294.
56. Y. Sasaki, K. Ohsawa, H. Kanazawa, S. Kohsaka, Y. Imai, *Biochem. Biophys. Res. Commun.* **2001**, *286*, 292.
57. J. Lier, W. J. Streit, I. Bechmann, *Cells* **2021**, *10*, 2236.
58. L. J. Schipper, L. J. Zeverijn, M. J. Garnett, E. E. Voest, *Cancer Discov.* **2022**, *12*, 1634.
59. M. Chamundeeswari, J. Jeslin, M. L. Verma, *Environ. Chem. Lett.* **2019**, *17*, 849.
60. M. C. Scicluna, L. Vella-Zarb, *ACS Appl Nano Mater* **2020**, *3*, 3097.
61. S. Krol, *J. Controlled Release* **2012**, *164*, 145.
62. F. Karimzadeh, K. Mahnam, M. Rezaee, F. Toghroli, R. Malekzadeh, F. Elahian, S. A. Mirzaei, *J Drug Deliv Sci Technol* **2025**, *110*, 107115.
63. R. Ganpisetti, S. Giridharan, G. S. S. J. Vaskuri, N. Narang, P. Basim, M. R. Dokmeci, M. Ermis, S. Rojekar, A. D. Gholap, N. Kommineni, *Biomolecules* **2025**, *15*, 802.
64. C. Shi, D. Guo, K. Xiao, X. Wang, L. Wang, J. Luo, *Nat. Commun.* **2015**, *6*, 7449.
65. D. Nuzzo, A. Girgenti, L. Palumbo, F. Naselli, M. Bavetta, G. Marfia, P. Picone, *Int. J. Mol. Sci.* **2024**, *25*, 12672.
66. P. Picone, D. Nuzzo, *Neural Regen Res* **2023**, *18*, 525.
67. P. Picone, *Int. J. Mol. Sci.* **2022**, *23*, 2245.
68. D. Nuzzo, P. Picone, *Int. J. Mol. Sci.* **2021**, *22*, 8866.

SUPPORTING INFORMATION

Additional supporting information can be found online in the Supporting Information section at the end of this article.

How to cite this article: M. Testa, L. Palumbo, M. La Rosa, A. Girgenti, F. S. Palumbo, P. Picone, F. Lopresti, D. Nuzzo, V. La Carruba, *VIEW*. **2026**, 20250211. https://doi.org/10.1002/VIW.20250211